

Centre for Aviation (ZAV)

Bachelor Thesis Industrial Engineering

Validation of 3D-Scanned Models for Aerodynamic Analysis and Real-Time Flow Visualisation

Author	Óscar Luis Domínguez
Supervisor	Wilm Friedrichs
Co-supervisors	Michael Ammann Tobias Zihlmann
Date	06.06.2025

Abstract

This thesis presents the validation of 3D-scanned models for aerodynamic analysis and the real-time visualisation of airflow using ProCap system.

Two main aspects are addressed regarding the validation of the 3D-scanned models. First, the visualisation performance within the ProCap software is evaluated, including the necessary steps for importing the model into the system. Second, a deviation analysis is conducted to assess whether the aerodynamic body—in this case, a GTA aeroplane model—meets the required tolerances, which are critical for ensuring a good aerodynamic performance. Additionally, the need to recreate the scanned surface is discussed, although without a specific practical case.

Concerning the ProCap system, this thesis explores its setup, its advantages and disadvantages, and its potential for aerodynamic studies. More precisely, two studies are carried out to observe the effects of varying the angle of attack: first on an aerofoil model and the second on a GTA aeroplane model.

All of the above is supported by the relevant theoretical foundations.

Acknowledgements

I would like to dedicate this thesis to my grandparents, especially my paternal grandmother, who had been looking forward to seeing me become an engineer, but sadly passed away recently. My grandparents have always been a great source of support, offering invaluable advice that only comes with age and experience.

I want to express my gratitude to my supervisor and co-supervisors: Wilm Friedrichs, Tobias Zihlmann and Michael Ammann, for their guidance and for trusting me with this thesis project.

I would also like to thank my parents for their unconditional support: for cheering me up, believing in me, advising me, and helping me through any challenge I face.

My brother also deserves a special mention for his patience, support and help whenever I have needed it.

Finally, I would like to thank all my closest friends, who are always there to listen, support, and share a laugh. I am very proud of them and feel privileged to have them in my life.

I also acknowledge the use of OpenAI's ChatGPT, which was used to improve grammar and style, clarify explanations, create the bibliography in LaTeX, and assist with technical aspects of LaTeX. All ideas, interpretations, the structure, and conclusions presented in this work are entirely my own.

Contents

1	Intr	oducti	ion	6
2	The	eoretica	al background	7
	2.1	Types	of 3D-scanning technologies	7
		2.1.1	Contact scanners	7
		2.1.2	Non-contact scanners	8
	2.2	Surfac	e waviness	11
	2.3	Measu	rement of surface waviness	12
	2.4	Effect	of surface waviness on aerodynamic performance	12
	2.5		rement system: iProbe	17
		2.5.1	Principles of operation	17
		2.5.2	Wall proximity effect	19
3	3D-	Scanni	ing for aerodynamics	21
	3.1	Use ca	ase: Flow visualisation	21
		3.1.1	Use case discussion	21
		3.1.2	ProCap system	21
		3.1.3	Workflow: From scan to STL	22
	3.2	Use ca	ase: Tolerance inspection	25
		3.2.1	Use case discussion	25
		3.2.2	Workflow: From scan to tolerance analysis	25
	3.3	Use ca	ase: Comparison with numerics	25
		3.3.1	Use case discussion	25
		3.3.2	Workflow: From scan to CAD	26
	3.4	Marke	et study on the types of scanners	26
4	Exa	mple a	applications	28
	4.1	Use ca	ase: Flow visualisation of aerofoil model	28
		4.1.1	Test 1: 0° angle of attack	32
		4.1.2	Test 2: 5° angle of attack	33
		4.1.3	Test 3: 10° angle of attack	36
	4.2	Use ca	ase: Flow visualisation of the GTA aeroplane model	37
		4.2.1	Test 1: 0° angle of attack	40
		4.2.2	Test 2: 5° angle of attack	43
		4.2.3	Test 3: 10° angle of attack	46
	4.3	Use ca	ase: Tolerance inspection of the GTA aeroplane model	48
		4.3.1	Scanning of the GTA model	48
		4.3.2	Tolerance analysis	51

5	Discussion of results	54
	5.1 Use case: Flow visualisation of the aerofoil model	54
	5.2 Use case: Flow visualisation of the GTA model	54
	5.3 Use case: Tolerance inspection of the GTA aeroplane model	56
6	Conclusion	58
\mathbf{A}	Scanners' Datasheets	64
В	Technical Drawing of the Aerofoil	73
\mathbf{C}	Creaform HandySCAN 700 Technical specifications	75

List of Figures

2.1	Different types of contact scanners (from [4])	8	
2.2	Time-of-flight method (from [10])	9	
2.3	Phase-shift method representation (from [10])	10	
2.4	Representation of the triangulation method (from [10])	11	
2.5	Definition of waviness (from [23])	12	
2.6	Effect of a 2D surface imperfection on the transition process of laminar		
	flow (from [25])	13	
2.7	Tollmien-Schlichting instability growth in the presence of a surface wave (from	[25])	1
2.8	Relationship between λ and h for different seat class civil aircraft (from [23])	16	
2.9	Geometry of common multi-hole pressure probes. (a), Two-hole yaw probe;		
	(b) three-hole yawstagnation probe; (c), five-hole cruciform probe (from [28]).	18	
2.10	Illustration of effect of Pitot tube on streamlines near a solid bound-		
	ary (from [30])	20	
3.1	From scan-to-CAD	24	
4.1	Screenshot of the aerofoil model in CATIA V5	29	
4.2	Component setup for the experiments	30	
4.3	Motive:Tracker software interface overview	31	
4.4	Position location of the aerofoil with 5° angle of attack	31	
4.5	Static pressure distribution with a 0° angle of attack	32	
4.6	Static pressure distribution at 0° angle of attack for comparison purposes .	33	
4.7	Absolute velocity distribution at 0° angle of attack	33	
4.8	Static pressure distribution with a 5° angle of attack	34	
4.9	Absolute velocity distribution in the upper region with a 5° angle of attack	35	
4.10	Absolute velocity distribution in the lower region with a 5 $^{\circ}$ angle of attack	35	
4.11	1	36	
	Absolute velocity distribution with a 10° angle of attack	37	
	GTA model with targets	38	
	Wind tunnel	39	
	Static pressure field around the GTA model	40	
	Absolute velocity distribution around the GTA model	41	
	Close-up view of the vortex formation behind the wingtip	41	
	x-component of the velocity field around the GTA model	42	
	Static pressure distribution around the GTA model at 5° angle of attack.	43	
	Absolute velocity distribution around the GTA model at 5° angle of attack	44	
4.21	Alternative view of the absolute velocity distribution showing the low-	4.4	
	velocity anomaly	44	

x-component of the velocity field around the GTA model at 5° angle of	
attack	45
Static pressure distribution for a 10° angle of attack	46
Absolute velocity distribution for a 10° angle of attack	47
x-component of the velocity field with a detailed view of the vortex	47
Interface of VXelements and visualisation of the scan	49
Process of scanning the lower part of the GTA model with the help of a	
targeted box	50
Interface visualisation of 3DEXPERIENCE with the original and the scanned	
model (in yellow)	52
Best Fit alignment	52
Model and scan after the fine tuning alignment	53
Streamline visualisation in ProCap	56
Deviation analysis of the GTA model	57
	Static pressure distribution for a 10° angle of attack Absolute velocity distribution for a 10° angle of attack

Chapter 1

Introduction

In recent years, 3D scanners have gained significant popularity due to their advanced capabilities and performance across various fields. This thesis aims to evaluate their performance and suitability within the context of aerodynamics. In parallel, we will assess a software tool called ProCap, which allows real-time visualisation of airflow around an object being tested in the wind tunnel. While there are various software options available, we have chosen ProCap because it is the tool accessible to us.

The primary objective of this work is to investigate the potential of 3D scanners to accurately recreate a model that can be imported into this ProCap software for visualisation purposes. Additionally, we aim to determine whether 3D scanners offer sufficient accuracy for tolerance inspection of the surface, and to study the relevance of such inspection. Finally, we will discuss the importance of reconstructing the surface from the scan. Finally, we will explore the importance of surface reconstruction from scanned data.

Regarding the ProCap software, several tests will be conducted by varying the angle of attack of an aerofoil and a GTA aircraft model. These experiments will help us to assess the capabilities of ProCap's measurement system in generating accurate and reliable aerodynamic data.

Throughout the project, not only will the 3D scanner and the ProCap software (or any other required tools) be tested, but a deep understanding of the underlying technologies, their advantages, limitations, and potential applications in aerodynamic engineering will also be pursued.

Chapter 2

Theoretical background

2.1 Types of 3D-scanning technologies

3D scanning devices are divided into 2 main categories [1]:

- Contact scanners
- Non-contact scanners

In other cases, an additional division is made for the non-contact scanners [2]:

- Active scanners
- Passive scanners

2.1.1 Contact scanners

This type of scanners uses probes that follow the physical surface. The probe is mounted on either a coordinate measuring machine (CMM) or a coordinate measuring arm (CMA). There are four basic types of CMM construction: gantry-type, bridge-type, cantilever-type, and horizontal arm-type. A key distinction between CMMs and CMAs is that the latter can operate outdoors, which is an advantage of CMAs over CMMs.

The probing process can vary depending on the application, machine type and required level of detail. Some systems use a single-point probe (recording one point at a time) while others use continuous scanning probes that collect a large number of data points along a continuous path.

In either case, the accuracy is excellent. However, achieving high levels of detail requires measurements to be taken in temperature-controlled environments. These systems tend to be relatively slow, as points are recorded sequentially by the probe. The speed of the process depends on the velocity of the probe. Additionally, because contact is required, they are not suitable for soft materials (which may deform under pressure, resulting in inaccurate data) or for fragile objects. Scanning complex geometries can also be challenging or even impossible. Another disadvantage is that these machines typically require long installation procedures [1][3][4][5][6].

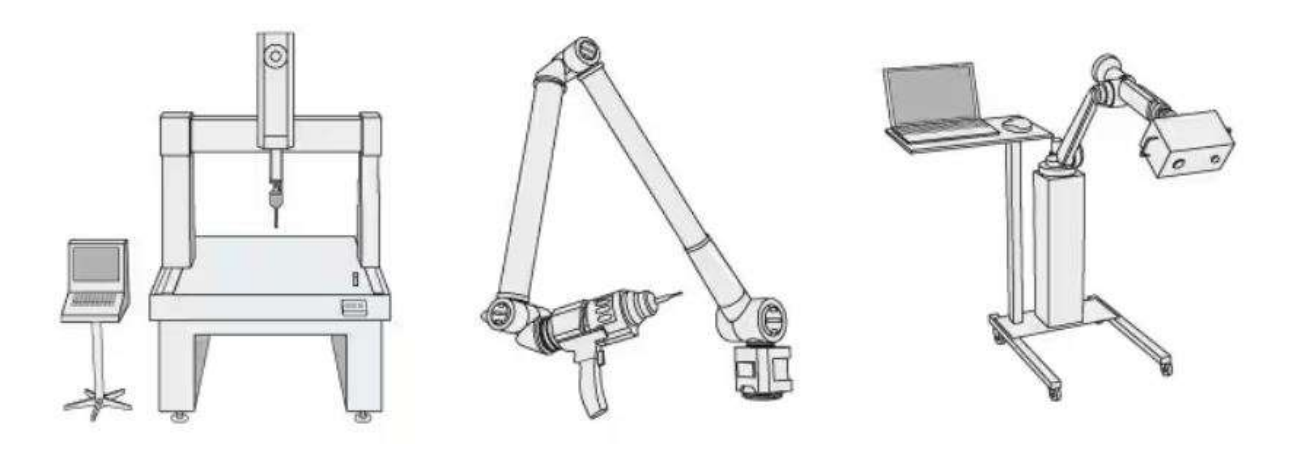


Figure 2.1: Different types of contact scanners (from [4])

2.1.2 Non-contact scanners

Non-contact passive scanners

In this case, scanners do not radiate energy onto the subject (the scanner does not emit its own light). Instead, it analyses natural ambient light. The cost of scanning with these scanners is the lowest, as it is not necessary to invest in specialised equipment [2][7]. Some examples of this type of techniques are:

- Stereoscopic Systems. It involves analysing the differences between images captured by two video cameras placed slightly apart, both looking at the same scene.
- Photometric Systems. Multiple images are captured under varying lighting conditions, typically by a single camera. This technique aims to invert the image formation model, which is a mathematical representation of how the image is generated. By inverting this model, the goal is to recover the surface orientation at each pixel.
- Silhouette Techniques. This technique uses outlines generated from the contrast between an object and a well-contrasted background in a sequence of photographs. The obtained shape is not an exact representation of the object. Moreover, this method cannot capture concavities of the object, as they are only based on the silhouette. However, the model together with color and texture information can have plenty of different applications [2] [8].
- Photogrammetry. This method consists of taking photographs with overlapping fields of view. Using software algorithms that identify and match points across multiple images, it is possible to reconstruct a 3D model based on those correspondences. This methodology is pretty similar to that of photometric systems. However, it is generally less precise, as the shadows and lighting variations used in photometric systems allow for a more accurate definition of surface detail—particularly when the surface contains curves or irregular shapes [9].

Non-contact active scanners

Non-contact active scanners emit and collect radiation (or light) reflected from the object's surface. The types of emissions commonly used include optical light (including

lasers), ultrasound and x-ray [2].

Non-contact active scanners techniques

The three most common techniques used in non-contact active 3D scanning are Time-of-Flight, phase-shift, and triangulation. While the physical principles behind these techniques can, in theory, be applied using different types of emissions—such as ultrasound or X-rays—they are most commonly implemented with laser, infrared light, or LED-based systems. Therefore, the following descriptions focus on optical systems, which are the standard in most 3D scanning applications.

• Time-of-flight systems (ToF) or pulse-based measurement systems. They use laser light to probe the subject. They work by emitting a single pulse of laser light and measuring the time it takes for the pulse to be reflected back to the scanner's sensor (Figure 2.2).

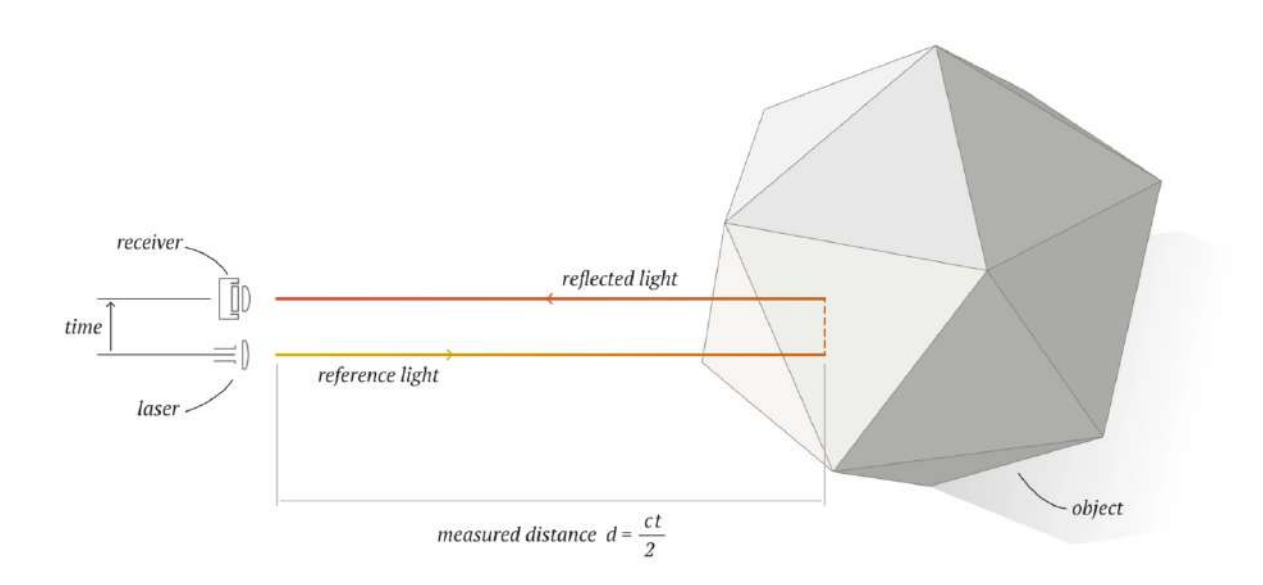


Figure 2.2: Time-of-flight method (from [10])

The laser range finder detects the distance of a single point in its line of sight. By changing its direction, the scanner can capture multiple points within its field of view. There are two methods for modifying the direction of the laser range finder: by rotating the range finder itself, or by using a system based on rotating mirrors. This last method is commonly used [2][10].

The precision of this kind of technology is estimated at 1% of the distance from the object. For instance, the accuracy for an object placed 5m away is around 5cm [11]. The measurement range goes from a few centimetres to several meters (6-8m)[12].

One of the main disadvantages of ToF cameras is that they do not work well outdoors or in britly-lit areas as the emitting light can be diminished by ambient light. They also do not perform well with highly reflective surfaces [13].

• Phase-shift systems (sometimes referred to as indirect ToF). This systems also use emitted laser light, but its intensity is modulated with a specific waveform. The scanner compares the phase shift of the reflected laser light to a standard one, which is also captured for comparison (Figure 2.3). This method ensure precise distance calculation [14].

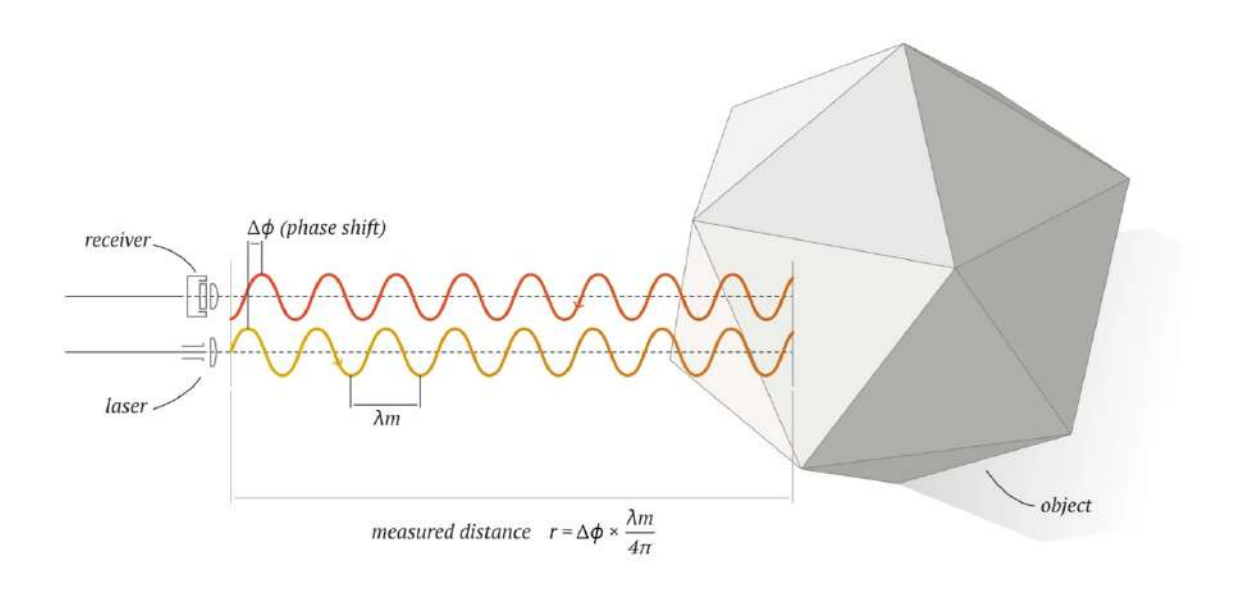


Figure 2.3: Phase-shift method representation (from [10])

Unlike time-of-flight systems that emit discrete light pulses, phase-based laser scanners produce a continuously modulated laser beam allowing for higher scanning speeds. However, this method is less accurate than ToF systems, as the resulting point clouds tend to be noisier [2][15].

• Triangulation-based scanners. Like the other methods, these scanners also use emitted laser light. They capture the reflected light with an on-board camera sensor. Depending on the distance of the object relative to the camera, the laser dots will appear at different positions in the camera's field of view. The laser dot, the camera and the laser emitter form a triangle, which is why this technique is called triangulation. The shape and size of this imaginary triangle are determined because the distance between the camera and the laser, the angle at the laser emitter and the angle at the camera are known. Most of the times, instead of using a single laser dot, a laser stripe is projected to speed up the scanning process. With this method, more than 1,000 scans per second can be performed [2][16].

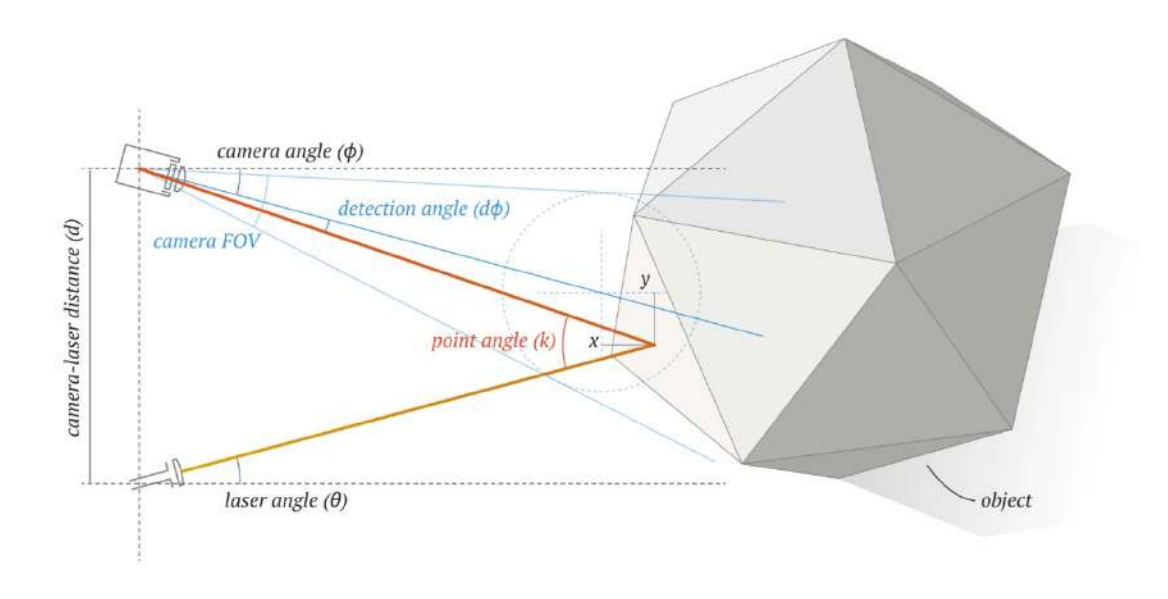


Figure 2.4: Representation of the triangulation method (from [10])

2.2 Surface waviness

Surface roughness describes how much a surface deviates from its ideal geometric form. Higher values indicate rougher surfaces, while lower values correspond to smoother ones [17]. In technical drawings, the specification of geometrical features, including surface roughness, follows the rules established in **EN ISO 1101**[18], which governs the Geometrical Product Specifications (GPS) system. This standard defines the way surface roughness symbols are represented on technical documentation.

Specifically, two different representations can be distinguished: the line profile, referring to a two-dimensional cross-sectional view of the surface, and the surface profile, corresponding to the three-dimensional topography. Within each category, two types of features are distinguished: integral and derived features.

The integral feature represents the actual, unaltered line or surface obtained directly from the measurement, without any mathematical adjustment. In contrast, the derived feature results from applying mathematical operations to the measured data in order to obtain a reference line or surface for analysis. The parameters that characterize surface roughness are formally defined in **ISO 4287**[19] (for line profile roughness, 2D) and **EN ISO 25178-2**[20] (for surface roughness, 3D).

In the field of aerodynamics, we will focus on waviness, which refers to the large-scale surface deviations that occur over long wavelengths. In contrast, roughness refers to small-scale irregularities occurring over short wavelengths. Although the aerodynamic effects differ significantly, with waviness generally having a greater impact on the flow [21], manufacturing standards or surface specifications often do not distinguish between the two, treating them as essentially the same.

2.3 Measurement of surface waviness

The procedure used in real-life applications is called **skin mapping**. One specific type is known as **Aircraft RVSM Skin Mapping**, which is conducted to ensure that the airframe condition meets the requirement for operating within RVSM (Reduced Vertical Separation Minimum) airspace. For simplicity, RVSM refers to a designated region of airspace where reduced vertical separation between aircraft is permitted.

To carry this inspection, specialised tools and equipment are required to measure the fuse-lage's surface and provide documented proof of compliance. Before beginning the skin mapping procedure, the aircraft needs to be properly prepared. This includes cleaning the surface, ensuring the aircraft is positioned on a level surface, and removing external equipment and devices that may interfere with the measurements. A **surface profilometer** is then used to collect the surface data. This is a specialised instrument used to measure the surface roughness of the fuselage. This device generates a high-resolution, three-dimensional map of the surface and can detect even minor deviations, for instance dents or waviness. Other tools can be also used for high-precision surface mapping, such as laser scanner, which accurately measures surface irregularities; a calibrated straight edge, which functions as a high precision reference ruler or as part of an electronic measuring system; and a feeler gauge, which can be used to measure the gap between the aircraft skin and the straight edge.

To determine the depth of any surface irregularity detected during the skin mapping process, instruments such as digital calipers or micrometers are employed.

Reference standards—either physical (such as gauge blocks or flat plates), or digital (stored within the electronic measuring devices)—are used to ensure accurate measurement. Finally, all collected data is recorded and compared against the manufacturer's specified limits for allowable skin waviness [22].

2.4 Effect of surface waviness on aerodynamic performance

As mentioned before, surface waviness plays an essential role in aerodynamic performance. Mathematically, waviness is defined as the ratio of wave height (h) to wavelength (λ) . In Figure 2.5, the parameter $\frac{h}{\lambda}$ is illustrated.

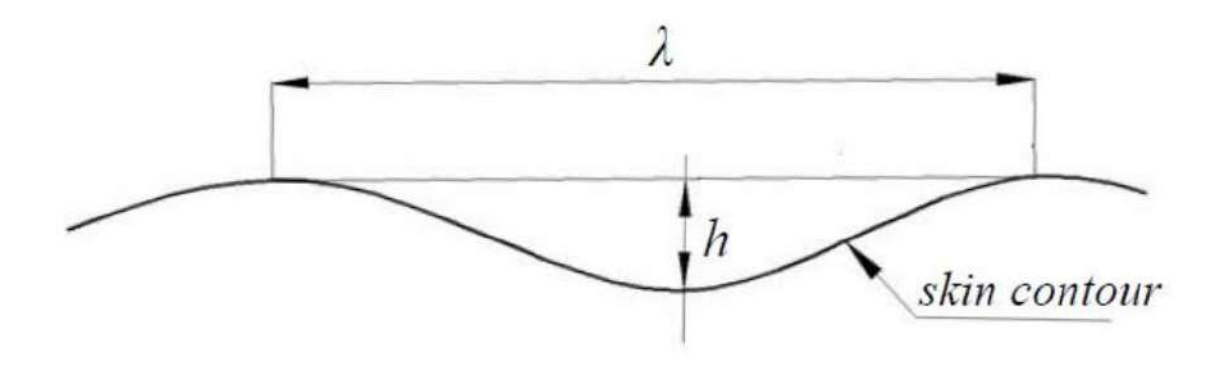


Figure 2.5: Definition of waviness (from [23])

Achieving the natural laminar flow (NLF) regime on airframe surfaces can reduce the total

drag by 7-16%. However, to do so, plenty of requirements will have to be fulfilled. From a geometrical perspective, important factors include restricting sweep angles to prevent transition governed by Tollmien–Schlichting (TS) waves, ensuring a favorable pressure gradient (pressure must decrease in the flow's direction), limiting the radius of the aerofoils' leading edge to avoid attachment-line instability, and ensuring compatibility with high-lift devices (such as Krüger flaps) to enhance performance and/or protect against insect interference [24].

We will focus exclusively on the Tollmien-Schlichting (TS) waves. When a given twodimensional imperfection is present, Figure 2.6 illustrates its possible effects on the transition process.

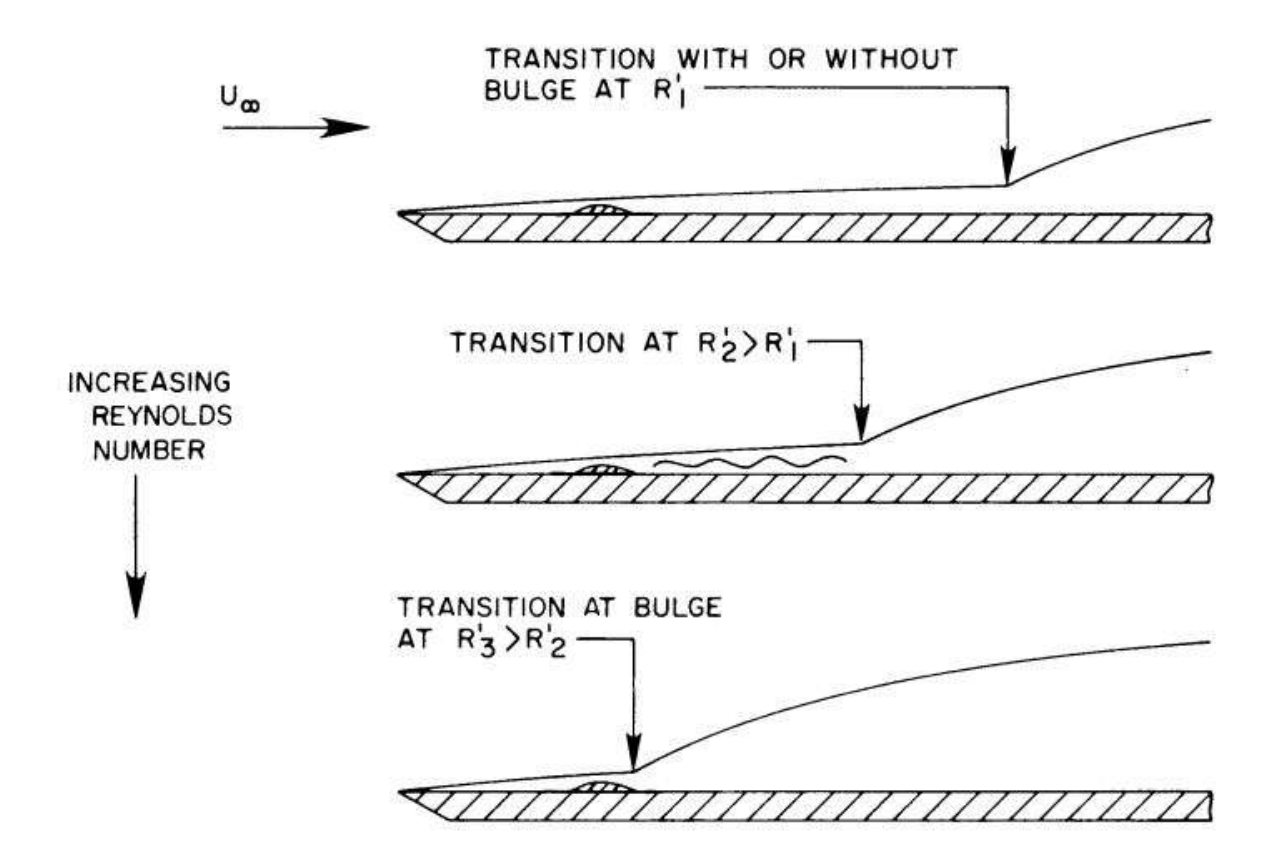


Figure 2.6: Effect of a 2D surface imperfection on the transition process of laminar flow (from [25])

In Figure 2.6, the top image represents a subcritical condition where the transition remains unaffected by the imperfection. The middle image shows the critical condition at which the transition just begins to be influenced by the disturbance. Finally, the bottom image illustrates a supercritical condition, where the imperfection causes a rapid amplification of T-S waves, leading to an early transition very close to the imperfection itself. As shown in Figure 2.6, the Reynolds number increases from the top image to the bottom one. Although we are discussing laminar flow regimes, it is important to note that the associated Reynolds numbers are very high, often reaching values up to 30 million for chord Reynolds numbers and around 14 million for transition Reynolds numbers, as observed in flight investigations [25].

[25] provides an example of Tollmien–Schlichting (TS) instability growth caused by a

surface waviness characterized by a wave height of $h = 0.254 \,\mathrm{mm}$ and a wavelength of $x = 63.5 \,\mathrm{mm}$. In Figure 2.7, the effect of such an imperfection, located in 0.10 < x/c < 0.13, on the amplification of TS waves is illustrated.

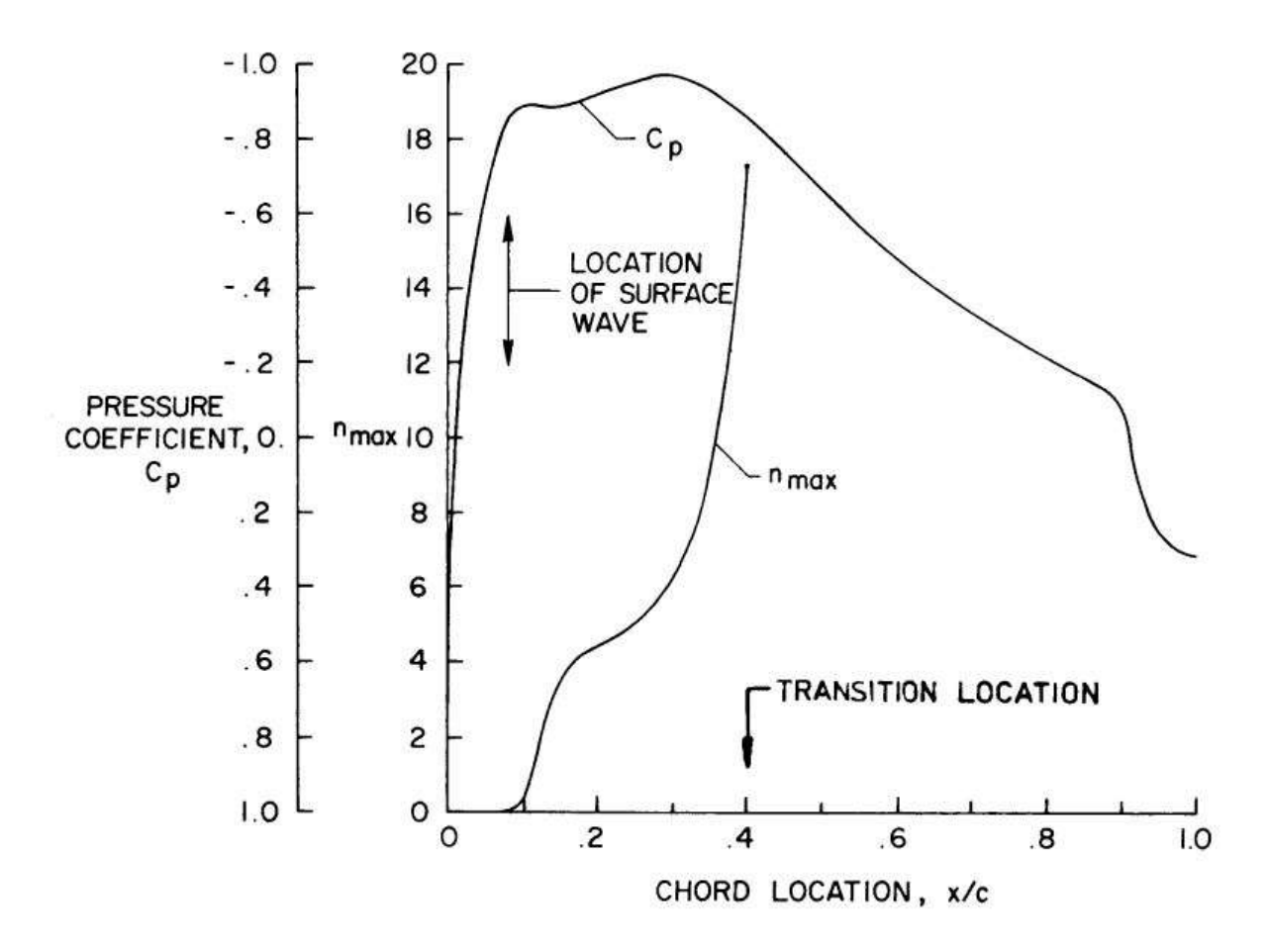


Figure 2.7: Tollmien-Schlichting instability growth in the presence of a surface wave (from [25])

The figure shows 2 different curves: One representing the n_{max} factor and the other the pressure coefficient, C_p . The vertical arrow indicates the position of the surface wave. Upon encountering this instability, we observe an adverse pressure gradient, where C_p becomes less negative, signifying flow deceleration. In this region, the n_{max} factor, which quantifies the amplification of the Tollmien-Schlichting wave, increases rapidly, rising from nearly 1 to approximately 4 within the small range of 0.10 to 0.13. Following this, the flow begins to accelerate again (C_p decreases, indicating a favourable pressure gradient), and the growth of the n_{max} factor slows down. However, before reaching the transition point, the pressure gradient becomes adverse again, accelerating the growth of the n_{max} factor. This renewed amplification ultimately leads to the breakdown of the laminar flow and the onset of turbulence

For this reason, a skin waviness requirement has been defined for civil aircraft, based on Carmichael's criterion. First, a sample must be taken from the dimensional measurement results, as waviness is a two-dimensional feature. Once this is done, the basic wave is obtained, allowing us to extract the characteristic parameters of the wave. The approximate wavelength range for each component is listed in Table 2.1.

Component	Wavelength		
Wing	100 mm - 800 mm		
Fuselage	100 mm - 650 mm		
Tail	80 mm - 450 mm		

Table 2.1: Wavelength range of each component [23]

The next step is to calculate the waviness requirement. This criterion is provided by Carmichael by the following formula:

$$\frac{h}{\lambda} = \left(\frac{59000 \cdot \cos^2(\Lambda)}{\lambda Re^{1.5}}\right)^{0.5}$$

Where h is the wave height in inches, λ is the wavelength in inches, c is the chord length in inches (the mean aerodynamic chord length can be used), Λ is the wing leading-edge sweep angle and Re is the Reynolds number based on the chord length and airspeed in the free-stream direction.

Solving the equation for h results in:

$$h = \left(\frac{59000\lambda \cdot \cos^2(\Lambda)}{Re^{1.5}}\right)^{0.5}$$

According to the formula, $\frac{h}{\lambda}$ depends on c, Λ , and Re. As c increases, the waviness requirement decreases, while Λ and Re increase the requirement.

The relationships between λ and h for different seat class civil aircraft are shown in Figure 2.8.

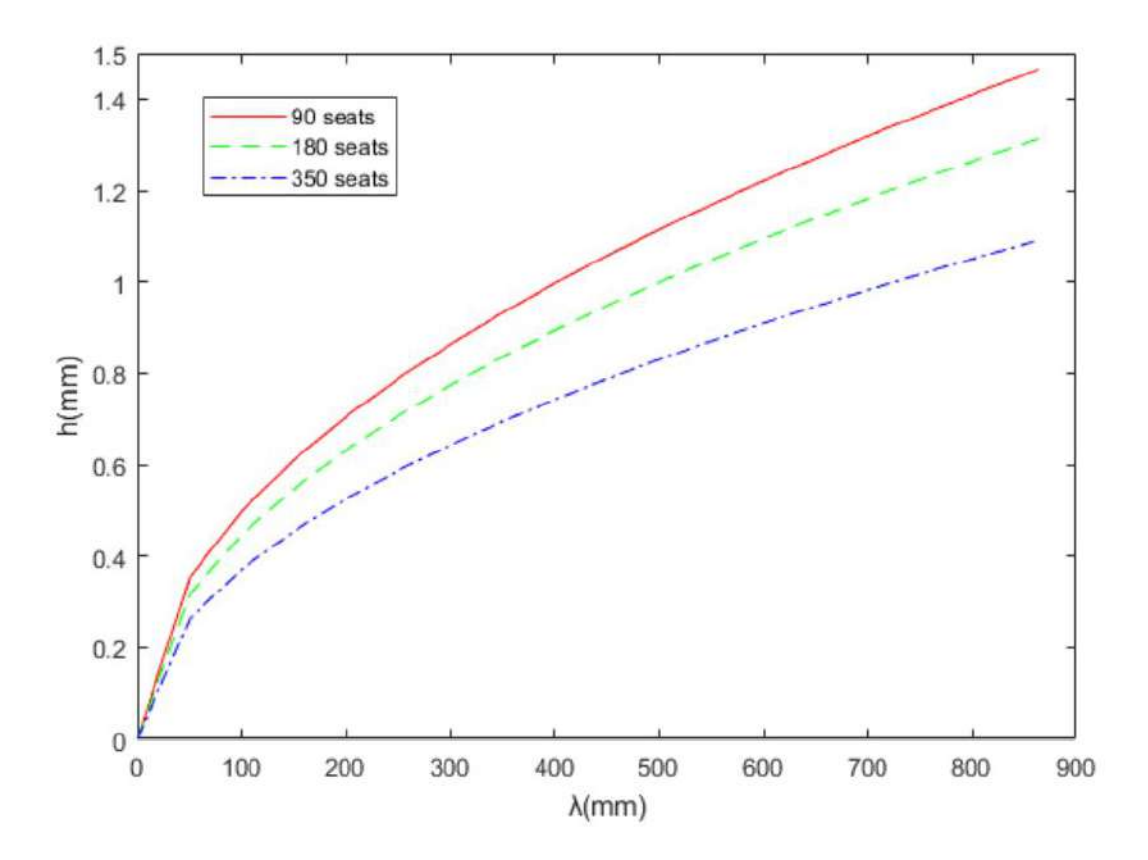


Figure 2.8: Relationship between λ and h for different seat class civil aircraft (from [23])

The range of maximum allowable waviness values for different types of civil aircraft can be obtained from Figure 2.8 and is summarised in Table 2.2

Type of Aircraft	Maximum allowed values of waviness
90 seats regional aircraft	0.0018 - 0.0056
180 seats single aisle aircraft	0.0015 - 0.0050
350 seats dual aisle aircraft	0.0013 - 0.0042

Table 2.2: Maximum allowed values of waviness for different types of civil aircraft [23]

All of the developments stated above are based on [23].

[26] states that another key difference between the real aircraft and a model lies in the influence of the atmosphere. At an altitude of 25,000 ft, the kinematic viscosity is approximately twice that at sea level. If we define the Reynolds number based on the kinematic viscosity:

$$Re = \frac{vl}{\nu}$$

where v is the velocity, l is the characteristic length (such as the chord length of an aerofoil) and ν is the kinematic viscosity. From this expression, it can be observed that as viscosity increases, the Reynolds number decreases. This leads to a higher tolerance for allowable waviness. However, in a wind tunnel, it is possible to achieve a lower kinematic viscosity than at sea level—for instance, as low as 1/15 of the free-stream value at sea level. This implies that the permissible waviness is more restrictive.

2.5 Measurement system: iProbe

In aerodynamic testing, where flow angle, speed, pressure and temperature need to be measured, multi-hole probes are commonly employed. Their design allows for precise measurements of flow parameters by capturing pressure data from multiple directions simultaneously. Multi-hole probes are often preferred over optical systems due to their relatively simple operation, lower maintenance requirements, and robustness in various applications.

The performance of multi-hole probes depends not only on their own characteristics—such as head geometry, number of holes, angular positioning of the holes, and sensitivity—but also on the properties of the measured flow field.

A five-hole probe is capable of measuring 3D unsteady flow and includes a calibration procedure to mitigate inertial effects caused by changes in flow velocity [27].

2.5.1 Principles of operation

A basic Pitot tube samples the local stagnation pressure (P_0) —the sum of static and dynamic pressure—at its central hole. It also measures the local static pressure P from side holes that are typically parallel to the flow. Since the probe sting might not be perfectly aligned with the flow, the static pressure P is usually taken as the mean value from multiple holes arranged circumferentially around the probe body.

The local mean velocity component parallel to the probe axis, denoted by U, can be then determined using Bernoulli's equation:

$$U = \left(\frac{2}{\rho}(P_0 - P)\right)^{\frac{1}{2}} \tag{2.1}$$

where ρ is the fluid density. The flow is assumed to be incompressible. The expression in Equation (2.1) is only valid when the flow is perfectly aligned with the probe axis, although it is not particularly sensitive to small misalignments.

For yaw angles greater than 10°, the pressure measured at the central hole is no longer considered to be under true stagnation conditions. Although the measured pressure is a complex function of the flow angle and the probe tip geometry, it can still be related directly to the flow angle through a single calibration function.

In this case we will consider a single, square-ended tube measuring flow with a velocity magnitude U and a yaw angle β relative to the tube axis. If $\beta = 0^{\circ}$, the pressure P_1 measured by the tube is equal to the stagnation pressure P_0 . Conversely, if $\beta = 90^{\circ}$, the pressure P_1 is equal to the static pressure P_{static} (P_S). For yaw angles in the range $0^{\circ} < \beta < 90^{\circ}$, the measured pressure P_1 will be between the stagnation pressure and the static pressure ($P_0 < P_1 < P_S$). The relationship between P_1 and β can be expressed through the following expression:

$$\beta = f_1 \left(\frac{2P_1}{\rho U^2} \right)$$

where f_1 is a continuous function defined for $0^{\circ} < \beta < 90^{\circ}$. In this formulation, the pressure P_1 has been normalised by the local dynamic pressure, $\frac{1}{2}\rho U^2$. This normalisation eliminates the effect of velocity on the function f_1 , making it velocity-insensitive. Thus, the relationship between the pressure ratio $\left(\frac{2P_1}{\rho U^2}\right)$ and the yaw angle β can be established without considering the actual velocity of the flow.

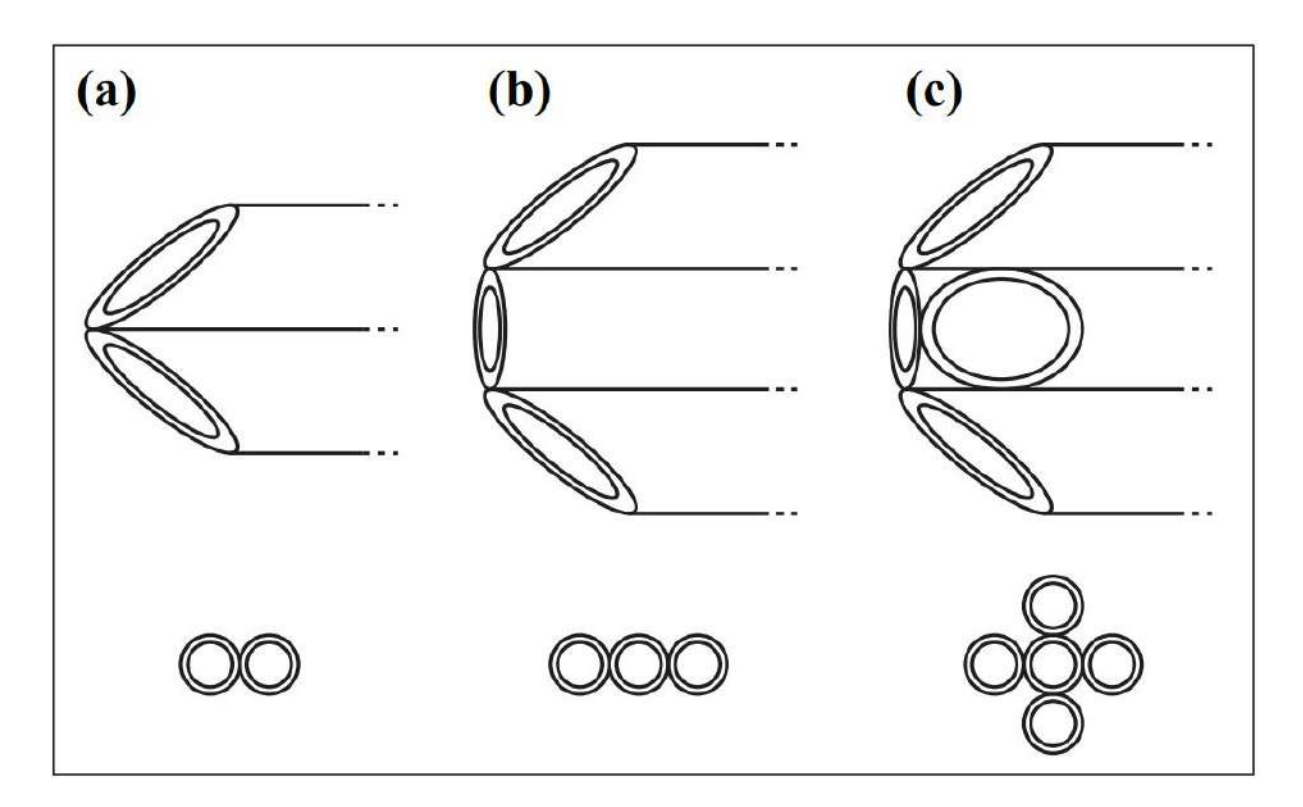


Figure 2.9: Geometry of common multi-hole pressure probes. (a), Two-hole yaw probe; (b) three-hole yawstagnation probe; (c), five-hole cruciform probe (from [28]).

If we extend this idea to three dimensions by combining five tubes in a cruciform arrangement, it is commonly known as five-hole probe, as illustrated in part (c) of Figure 2.9. The calibration space of the five-hole probe can be expressed as:

$$\alpha = f_1 \left(\frac{2P_1}{\rho U^2}\right) \quad P_1 < P_3$$

$$\alpha = f_3 \left(\frac{2P_3}{\rho U^2}\right) \quad P_3 < P_1$$

$$\beta = f_2 \left(\frac{2P_2}{\rho U^2}\right) \quad P_2 < P_4$$

$$\beta = f_4 \left(\frac{2P_4}{\rho U^2}\right) \quad P_4 < P_2,$$
(2.2)

where α is the pitch angle and β the yaw angle. The index '5' refers to the central hole, and the indices '1' through '4' indicate the peripheral holes, arranged in a counter-clockwise direction starting from the bottom. The static and stagnation pressures can be approximated as

$$P_0 \approx P_5$$

$$P_S \approx \overline{P} = \frac{1}{4} \sum_{i=1}^4 P_i. \tag{2.3}$$

The system defined by Equation (2.2) and Equation (2.3) presents two significant limitations. First, the calibration process requires the determination of 4 independent functions through calibration. Second, the approximations for P_0 and P_S are relatively inaccurate.

The first limitation can be resolved by reformulating the calibration functions. The pressure difference between opposing holes is also sensitive to flow angularity, as is the pressure at the individual holes, but over a smaller range of angles. We will define the pitch and yaw coefficients, $C_{P\alpha}$ and $C_{P\beta}$, using Equation (2.1) and Equation (2.3) to express the dynamic pressure in terms of the available pressures.

$$C_{P\alpha} = \frac{P_3 - P_1}{P_5 - \overline{P}}$$

$$C_{P\beta} = \frac{P_4 - P_2}{P_5 - \overline{P}}$$
(2.4)

This Equation (2.4) is more sensitive to the flow angle than Equation (2.2). To address the error between the approximate static and stagnation pressures used, the difference between the approximate and actual static and stagnation pressures can also be obtained through calibration. These differences are then normalized against the approximate dynamic pressure and expressed as nondimensional coefficients.

$$C_{P0} = \frac{P_5 - P_0}{P_5 - \overline{P}}$$

$$C_{PS} = \frac{\overline{P} - P_S}{P_5 - \overline{P}},$$
(2.5)

where the values of P_0 and P_S can be obtained from the measurement plane. Several calibrations are carried out at a series of known angles (α, β) in a flow with a fixed, known velocity U. The four coefficients $(C_{P\alpha}, C_{P\beta}, C_{P0}, C_{PS})$ at each (α, β) are recorded. The defined function relating the variables from the calibration data set is

$$\alpha = f_{\alpha} (C_{P\alpha}, C_{P\beta})$$

$$\beta = f_{\beta} (C_{P\alpha}, C_{P\beta})$$

$$C_{P0} = f_{0} (C_{P\alpha}, C_{P\beta})$$

$$C_{PS} = f_{S} (C_{P\alpha}, C_{P\beta})$$
(2.6)

For any given set of five pressures measured in a flow with unknown angularity and magnitude, the coefficients $C_{P\alpha}$ and C_{PS} can be determined from the experimental data using Equation (2.4). The flow angles (α, β) and the coefficients (C_{P0}) and (C_{PS}) can be obtained from Equation (2.6). Finally, the velocity magnitude can be obtained from the interpolated values of (C_{P0}) and (C_{PS}) by changing the definitions in Equation (2.6) for $(P_0 - P_S)$. We obtain the formula of the velocity:

$$|V| = \left(\frac{2}{\rho} \left(P_5 - \overline{P}\right) \left(C_{PS} - C_{P0} + 1\right)\right)^{\frac{1}{2}},$$

where |V| is the magnitude of the velocity vector [28] [29].

2.5.2 Wall proximity effect

Multi-hole probes are strongly affected by wall proximity, which impacts the accuracy of the pressure probes. Two main effects are responsible for this: the near-wall effect and the boundary layer effect. The near-wall effect is caused by the interference of the probe with the natural flow very close to the surface. By blocking the flow underneath the probe, the shear-induced streamline deflection is altered, deviating from its natural pattern caused by the vertical velocity gradient (Figure 2.10) [30]. This proximity causes the probe to measure a flow that appears to diverge from the wall. The effect becomes significant when the probe is placed closer than two diameters from the wall. Although this effect can be partially mitigated by the increased shear within the boundary layer, the induced error in flow angle measurements becomes unacceptable very quickly. The yaw angle measurement error can reach up to 0.7° for a yaw angle of 5°.

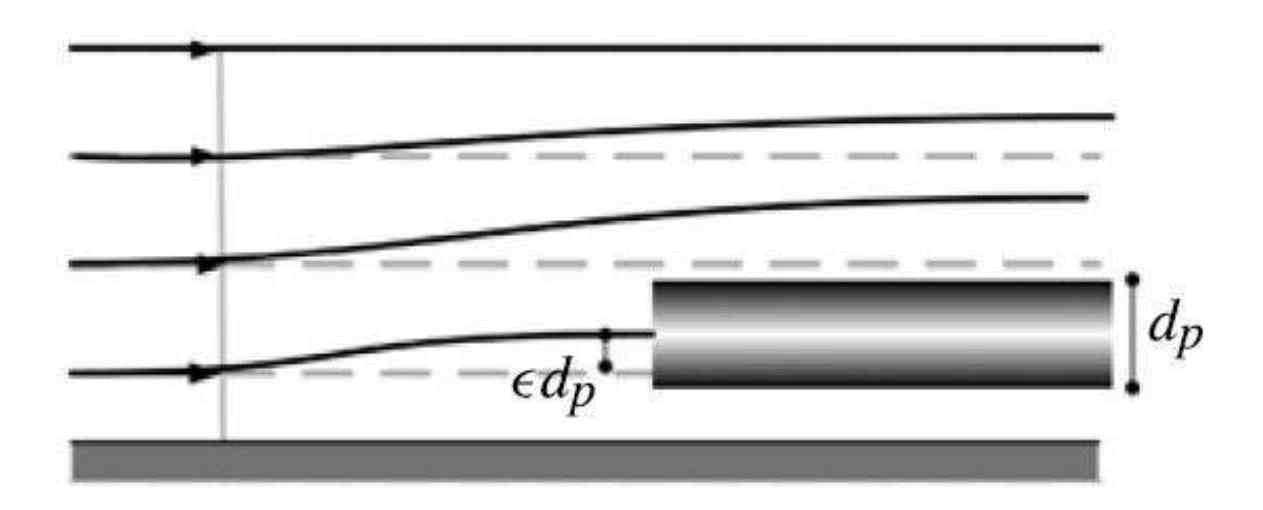


Figure 2.10: Illustration of effect of Pitot tube on streamlines near a solid boundary (from [30])

As mentioned earlier, the boundary layer effect can counteract the one caused by the wall proximity. In certain conditions, one effect may compensate for the other. When the two effects are isolated, the influence of the boundary layer on yaw angle measurements is found to be two or three times weaker than the wall proximity effect. The boundary layer reinforces the wall proximity effect when the probe has a negative pitch relative to the wall, while for a positive pitch, the boundary layer reduces the error. However, this compensating effect becomes less pronounced as the boundary layer thickens [31].

Chapter 3

3D-Scanning for aerodynamics

3.1 Use case: Flow visualisation

3.1.1 Use case discussion

One of the many applications of 3D scanners is visualization. These devices allow us to replicate a real-life object in a digital environment. In the context of aerodynamics, this capability is particularly valuable, as model visualisation is essential for correctly using the ProCap software as intended. Although ProCap can operate without a 3D model, doing so requires significant manual effort to locate, reorganise, and align the acquired data with the real-world object. This approach is not recommended, as it defeats the purpose of using the software efficiently.

3.1.2 ProCap system

As it is stated in their user's manual: "ProCap (from Probe Capture) is a real-time flow visualization system to map, process and display the 3D-flow topology as a direct feedback to the user while measurement is taking place" [32]. The data is captured using a point measurement probe—in our case the iProbe (a 5-hole probe with 1 kPa sensor option which can measure speeds up to 40.5 m/s)—which will be operated manually. The position data of the probe is processed using an optical tracking system. This allows the system to provide a time-averaged flow field on a regular grid in real-time. Data can be processed within the ProCap software or externally; in our case, we will use the ProCap software.

One of the main advantages of using ProCap is its intuitive operation and the realtime visual feedback of both the probe's position and the flow field. Some of the main applications of this system include:

- Flow investigation on complex geometries.
- Teaching and education.
- Building aerodynamics.

The ProCap measurement used in this work consists of the following components:

Item	Comment		
Digital multi-hole flow probe (iProbe)	L_5HPTCD_auut54_22 (1 kPa) (vectorflow)		
Tracking camera	V120:trio		
Measurement Laptop	Used to run ProCap software and process data		
Tripod	It supports the tracking camera		
Cables	Connection cables for all devices		

Table 3.1: Summary of 3D Scanning Use Case for Aerodynamics

3.1.3 Workflow: From scan to STL

The process starts by scanning the object. The scanner itself generates a STL file (or a similar format, such as OBJ). Internally, several methods are automatically executed.

First of all, the point cloud is filtered. The initial point cloud is composed by available points and noise points. Those noise points will lead to low accuracy for the subsequents surface reconstruction methods. There are two main sources of point cloud noise:

- The system error of the 3D scanning system.
- Environmental factors during data acquisition.

This noise can be divided into the following types: scattered noise, outlier gathering noise, internal repeated noise and redundant noise [33]. There are serveral noise removal methods. [33] mentions statistical filtering and radius filtering.

- The statistical filtering method uses the 3σ theory from probability. It calculates the average distance between each point and its neighbours within a specified range. Points that significantly deviate from this average are considered outliers and removed.
- Radius filtering method: It defines a sphere around each point, using a specific radius (from data). The number of neighbouring points within this sphere is counted. If the count is over a certain limit, the point is retained; otherwise, it is removed. This method filters points based on the local density of the point cloud.

Additionally, there are other methods such as outlier detection, moving least squares (MLS) and bilateral filtering (local surface fitting); feature-preserving filtering (no local filtering) [34] or deep learning de-noising [35].

The next step consists of extracting feature points from the point cloud to simplify the dataset. The method is based on Principal Component Analysis (PCA), where the normal vector of the point cloud is computed. Then, feature points are extracted based on the normal vector. This process reduces the number of points while preserving the shape of the geometric features of the point cloud [33].

Once this process is completed, the point cloud data processing begins. It consists of point cloud segmentation based on region growing and clustering and point cloud data extraction based on grid point offset. The first method divides the overall point cloud into separate regions to facilitate model reconstruction in those regions. The second method determines the order and position of the cloud data prior to data smoothing for surface reconstruction. The grid offset method is used to sort and filter the point cloud.

The final step to obtain the triangular patch model is the surface reconstruction of the point cloud by sub-areas through the determination of NURBS surfaces. As previously stated, this process is entirely performed by the laser scanner software. We obtain the STL file as the scanner's output, which represents the triangular patch model. It is important to highlight that the STL file only contains the triangulated mesh representation, and any NURBS surface information used during the reconstruction process is lost in this conversion.

From this point onward, the workflow diverges depending on the intended application. Since our objective is to reconstruct the object specifically for visualisation purposes within ProCap, no further processing steps are required, as the STL file is the format expected by the software.

All the steps mentioned above can be summarised in Figure 3.1

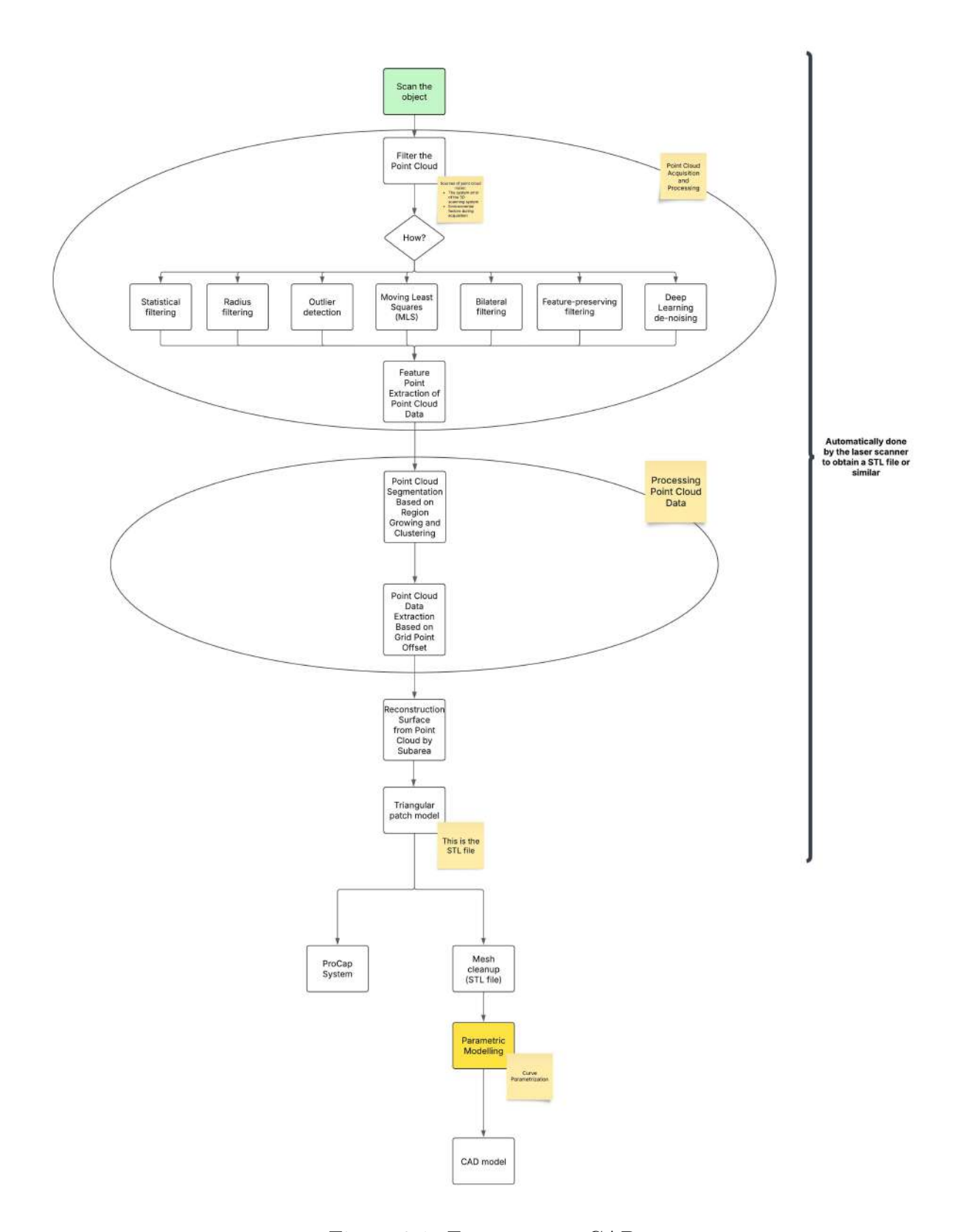


Figure 3.1: From scan-to-CAD $\,$

3.2 Use case: Tolerance inspection

3.2.1 Use case discussion

As shown in section 2.4, surface waviness plays a critical role in aerodynamic performance. Although we are working with scale models—where tighter tolerances would typically be expected—we will instead use tolerance values representative of real aircraft. This choice is made to align our analysis with real-world applications in the aviation industry, where such tolerances are relevant and practically implemented.

For instance, if we consider a 90-seat regional aircraft from Table 2.2 with a maximum allowed waviness value of 0.003 (taken as a midpoint between the two limit values) and we analyse the wing with a wavelength $\lambda = 100mm$ we can calculate the maximum allowable wave height as follows:

$$h = \frac{h}{\lambda}\lambda = 0.003 \cdot 100mm = 0.3mm$$

Thus, the maximum allowable wave height is h = 0.3mm.

We would like to check whether our model aircraft meets this requirement for the entire surface of the plane, not just the wings. As stated earlier, this tolerance is not the actual one that should be applied, but rather a symbolic representation of the full process that would be carried out to address this issue using a 3D scanner.

3.2.2 Workflow: From scan to tolerance analysis

The initial part of the workflow, from scanning to obtaining the STL file, is identical to the process described previously in section 3.1.3. In this case, we only require the STL file, so no further steps are necessary.

For tolerance analysis, it is essential to have access to the original CAD model (for instance, a .stp file). The analysis must follow a few established general steps:

First, both the CAD model and the STL file must be imported into the software to be used—in our case, 3DEXPERIENCE).

Next, both models need to be aligned. This step varies depending on the geometry you are working with, so general guidelines cannot be provided. Detailed instructions specific to the GTA airplane model used in this project will be presented in chapter 4.

Finally, the software automatically performs the deviation analysis between the ideal CAD model and the scanned STL file. It should be noted that the deviation value used to assess tolerance includes the combined contribution of all errors introduced during both the manufacturing and scanning process.

3.3 Use case: Comparison with numerics

3.3.1 Use case discussion

In this final use case, another application of 3D scanning is explored: comparing the performance of the original CAD model in a Computational Fluid Dynamics (CFD) simulation with that of a reconstructed model obtained from a 3D scan.

This approach allows us to evaluate the validity of using 3D-scanned geometry for CFD analysis in situations where the original CAD model is unavailable and reverse engineering

is required. An alternative application could be the comparison between CFD results and wind tunnel measurements of the scanned object, to assess whether both methods have consistent aerodynamic behaviour.

It must be emphasised that although CFD simulations can be carried out using STL files, CAD files (such as STEP files) are generally preferred due to their higher stability and robustness. Moreover, the geometry must be free of defects [36]. In most CFD tutorials, the workflow starts from a CAD model which is then exported to STL format. This means that all the original geometric information is available from the beginning—something we lack when working with scanned models. This is the main reason why reconstructing the CAD model from the scan is often necessary

3.3.2 Workflow: From scan to CAD

In this case, the method diverges from the previous two use cases. Since a CAD model is required for the CFD simulation, two additional phases must be carried out, as stated in [37].

The first additional phase is the mesh clean-up of the STL file. This is done to correct imperfections, fill holes, and remove unnecessary details. There are specific software tools for this task.

The second additional phase involves the parametric modelling of the surface, where curves are parametrized and used to generate NURBS surfaces, resulting in a ready CAD model.

This divergence in the workflow is also illustrated in Figure 3.1. In real-world scenarios, this process is manually carried out using software that enables the recreation of surfaces based on the triangular STL mesh. Because it is performed manually, the outcome depends heavily on the engineer's skill, and no general guidelines can be given—it also depends on the geometrical complexity of the object. For example, reconstructing the surface of the GTA airplane model, which will be used for tolerance analysis, would take approximately three to four working days for a professional engineer. This process would take even longer for someone with less experience. This information was provided by an expert in 3D scanning, P.Hug [38], from the ZHAW School of Engineering.

Due to time constraints, this section will not be addressed through a practical case in chapter 4.

3.4 Market study on the types of scanners

A market research has been conducted to identify the most commonly used 3D scanners for small-, medium-, and large-scale applications. The findings are summarised in Table 3.2 and Table 3.3.

Scanner (Brand)	Light source	Accuracy	Maximum Field of View (FOV)	Price	Comments
EinScan SP V2 (Shining 3D)	White LED	0.05mm	700 x 700 x 700mm	Around 2,000€	5kg maximum turntable load
Artec Micro II (Artec 3D)	RGB LED	0.005mm	200 x 200 x 150mm	24,800€	Scan-to-CAD option
Revopoint POP 2 (Revopoint)	Class 1 IR Camera	0.05mm	210 x 130mm (Single Capture Range)	550€	Handheld and turntable scanner. Targets required. Scanning spray needed for transparent, dark or highly reflective objects.

Table 3.2: Small and medium scale 3D scanners

It should be emphasised that lasers in Table 3.2 are not laser scanners. The three of them use structured light technology. They use the triangulation principle [39].

Scanner (Brand)	Light source	Accuracy	Maximum Field of View (FOV)	Price	Comments
T-SCAN hawk 2 (Zeiss)	Multiple blue laser crosses	$\begin{array}{ccc} 0.02 & \text{mm} & + \\ 0.015 & \text{mm/m} \\ \text{(volumetric)} \end{array}$	Adjustable resolution and field of view. Not specified in datasheet.	\$40,000	No coded markers required in satel- lite mode
3D Leica RTC360 LT (Leica Geosys- tems)	Laser class 1	1.0 mm + 10 ppm (range ac- curacy)	360° (horizontal) / 300° (vertical)	\$79,726.65	Coded markers are not required thanks to the Visual Inertial System
MetraSCAN 3D Black Elite (Creaform)	30 blue laser lines (+1 ex- tra line)	0.025 mm; Volumetric (16.6 m³): 0.078 mm	310 x 350 mm	\$93,000	360° magnetic targets for easy setup and dynamic tracking

Table 3.3: Medium and large scale 3D scanners

Chapter 4

Example applications

4.1 Use case: Flow visualisation of aerofoil model

For this practical application, a symmetrical NACA 0015 aerofoil was designed using CATIA V5 and subsequently manufactured using a 3D printer for testing in a micro wind tunnel, which consists primarily of a centrifugal blower. All these aspects will be discussed in detail.

For the symmetrical aerofoil sections, the following formula was used:

$$\pm \bar{y}_t = 5\bar{t} \left(A\sqrt{x} - B(\bar{x}) - C(\bar{x})^2 + D(\bar{x})^3 - E(\bar{x})^4 \right)$$

where $\bar{x} = \frac{x}{c}$, $\bar{y}_t = \frac{y_t}{c}$, and $\frac{t}{c} = \bar{t}$. Here, c is the chord length. The coefficients A to E were obtained through curve fitting to match the best-known aerofoils profiles, normalised to the same thickness-to-chord ratio. Their values are: A = 0.2969, B = 0.1260, C = 0.3516, D = 0.2843 and E = 0.1015. The $\pm \bar{y}_t$ refers to the upper $(+\bar{y}_t)$ and lower $(-\bar{y}_t)$ surfaces of the section. The thickness-to-chord ratio, denoted by \bar{t} , is $\bar{t} = 0.15$ for NACA 0015. The last parameter to be defined is the chord length, c, which must be specified. We will use $c = 99\,\mathrm{mm}$, as this corresponds to the diameter of the mounting hole used to hold the model in the micro wind tunnel. The aerofoil will be 128 mm tall and its profile will consist of 858 points. It will be mounted on a cylindrical base with a diameter of 99 mm and a height of 8 mm. The model is shown in Figure 4.1. The technical drawing is presented in appendix B.

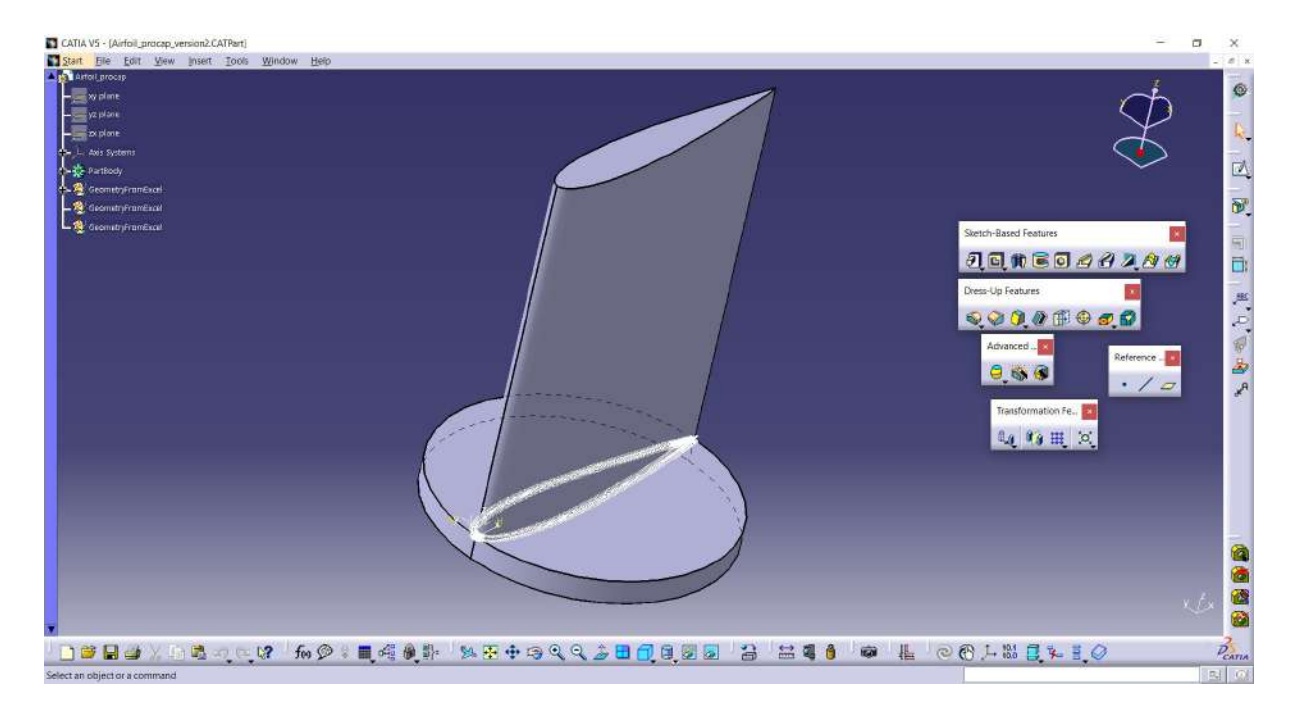


Figure 4.1: Screenshot of the aerofoil model in CATIA V5

Once the design was completed, the model was 3D printed. This process had to be repeated, as the first print resulted in a stepped surface that lacked the desired smoothness. For the second attempt, we increased the number of points to 858 points for the spline and we set the minimum point separation in the 3D printing software. This allowed us to produce a much more accurate model, suitable for use in ProCap.

The next step was to prepare the setup for testing using ProCap. To do this, we first had to connect all the equipment and position the optical camera such that the three reflective bubbles on the micro wind tunnel were visible in a software tool called Motive:Tracker, which must be used before launching ProCap (Figure 4.3). The position of the camera and two of the three reflective markers on the micro wind tunnel is shown in Figure 4.2. Motive:Tracker is essential for tracking the movement of the probe relative to a predefined reference frame. Once the three markers are visible in each of the three camera views within Motive:Tracker (Figure 4.3), we select these three points along with the camera representation in the Perspective view, and set them as the ground plane using the 'Set ground plane' button located on the right-hand side of the interface. This process establishes a reference coordinate system, allowing the probe's position to be accurately tracked throughout the experiment.

After setting up the reference system, the STL file of the aerofoil model had to be imported into ProCap. Due to time constraints, a 3D scanner was not used to create the STL file. In this case surface reconstruction was not necessary since the file was intended only for visualisation, so it was exported directly from CATIA V5. The coordinate system of the model is located just above the circular base and aligned with the leading edge of the aerofoil, as shown in Figure 4.1. This setup was not ideal, as it required considerable effort to reposition the aerofoil correctly within the software environment, especially after importing the micro wind tunnel model. Figure 4.4, shows the position of the aerofoil's local coordinate system relative to the global reference frame when set at an angle of attack of 5°.



Figure 4.2: Component setup for the experiments ${\cal C}$

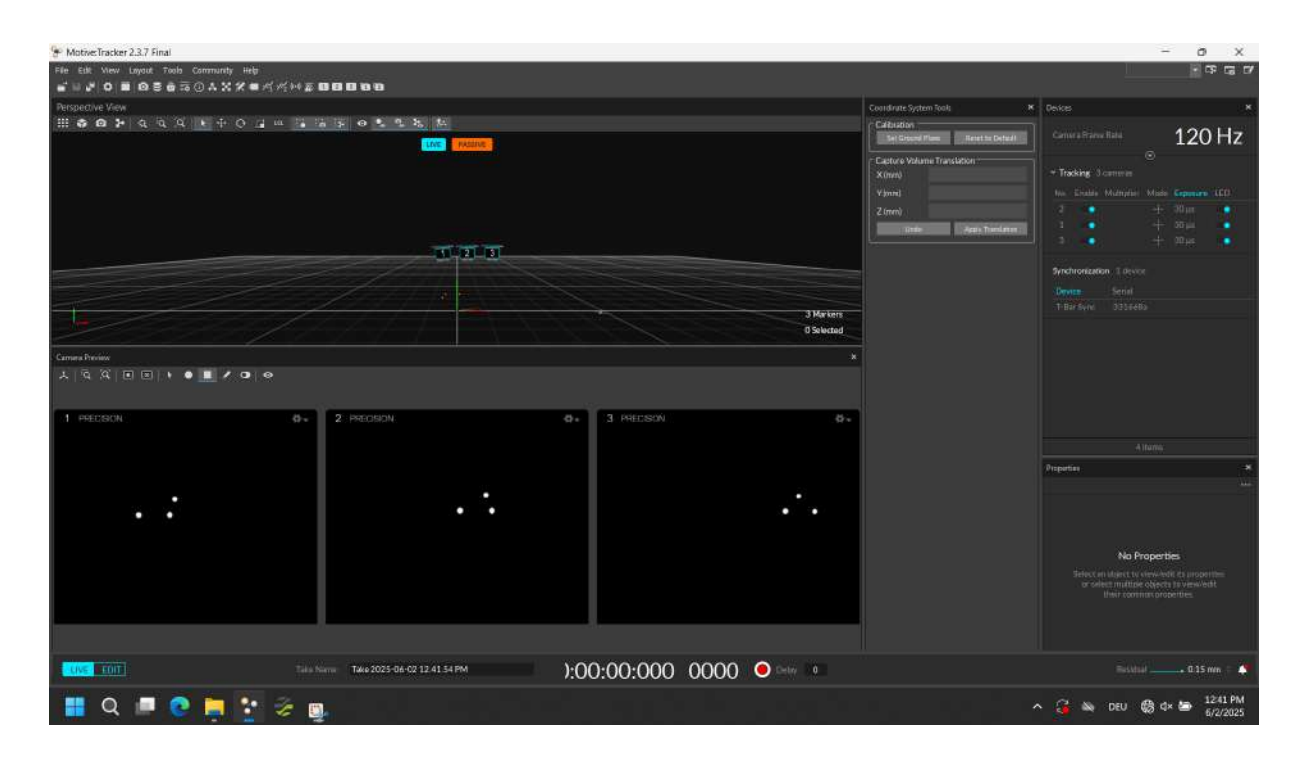


Figure 4.3: Motive:Tracker software interface overview

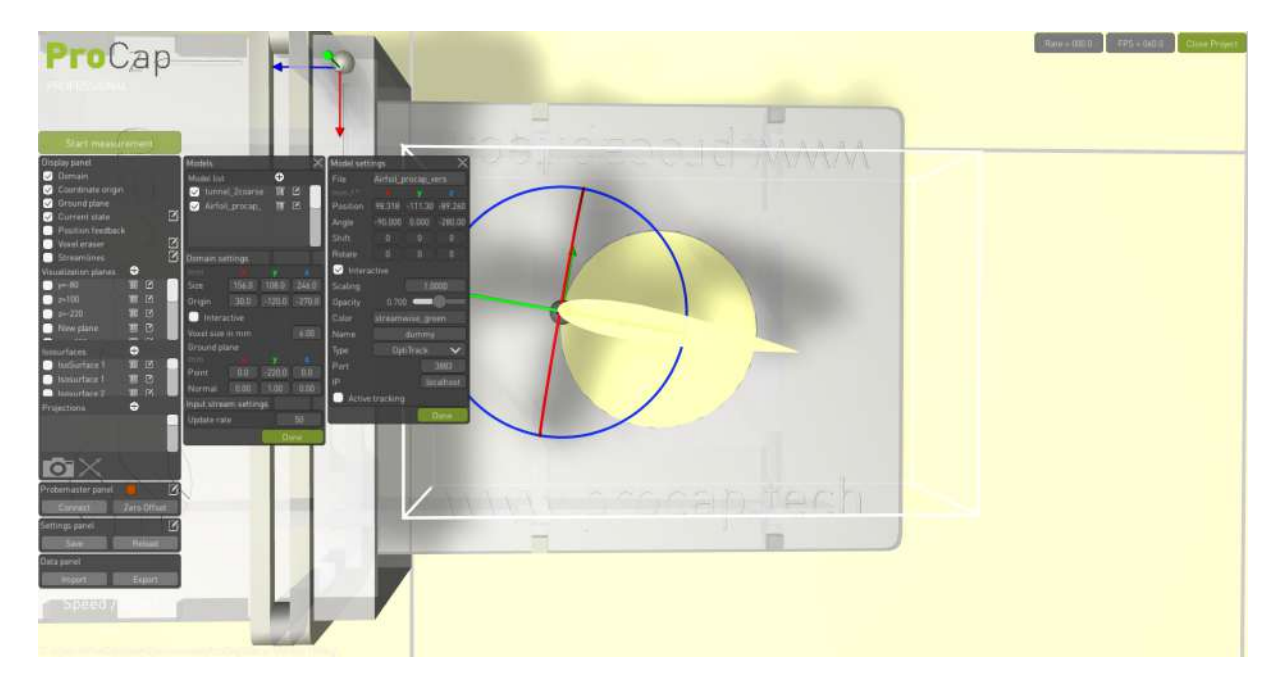


Figure 4.4: Position location of the aerofoil with 5 $^{\circ}$ angle of attack

Three different tests were carried out to observe the effect of varying the angle of attack: first at 0° , then at 5° and finally at 10° . In each case, the visualisation focuses on the static pressure (P_{stat}) and the absolute velocity vector projected onto the measurement plane, allowing both its magnitude and direction to be analysed.

4.1.1 Test 1: 0° angle of attack

When the aerofoil is positioned at a 0° angle of attack, the static pressure distribution shown in the Figure 4.5 indicates that the pressure is roughly equal on both the upper and lower surfaces of the section. This suggests that no significant lift is being generated due to pressure differences. For comparison purposes, we will use the same scale for all three tests in order to visualise any potential differences between them. In this case, adapting the pressure distribution to the general scale results in some loss of detail, but it provides a consistent basis for comparison.

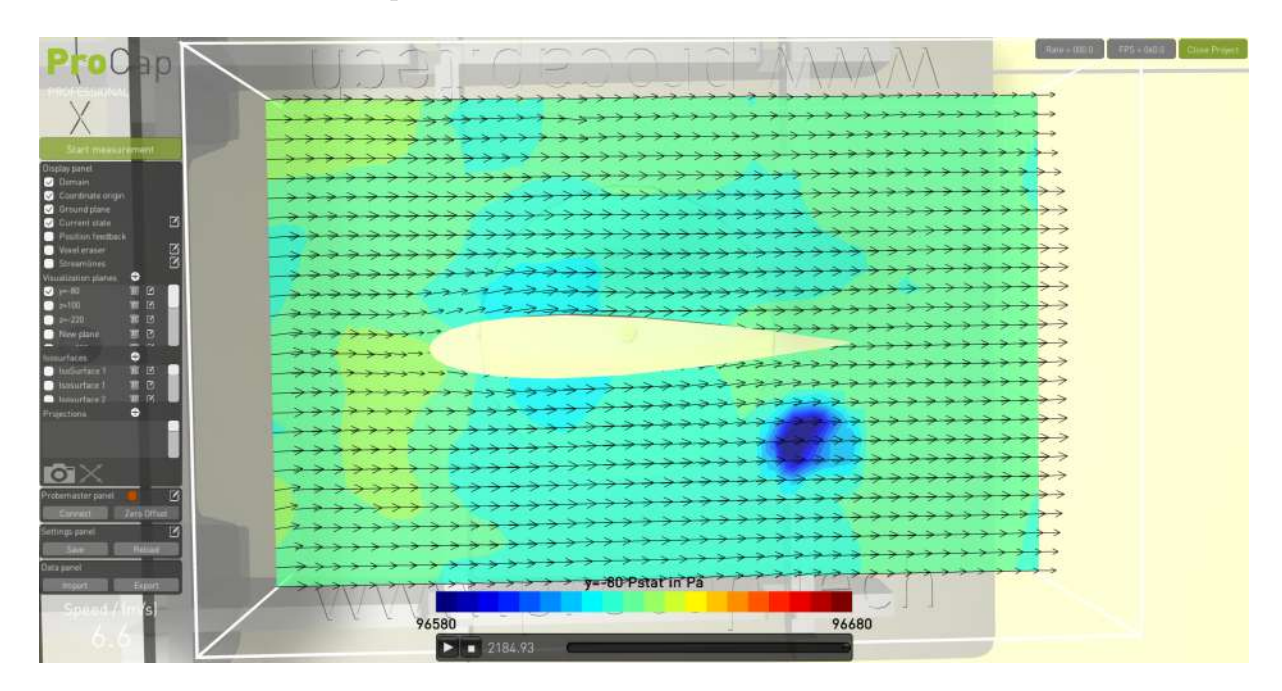


Figure 4.5: Static pressure distribution with a 0° angle of attack

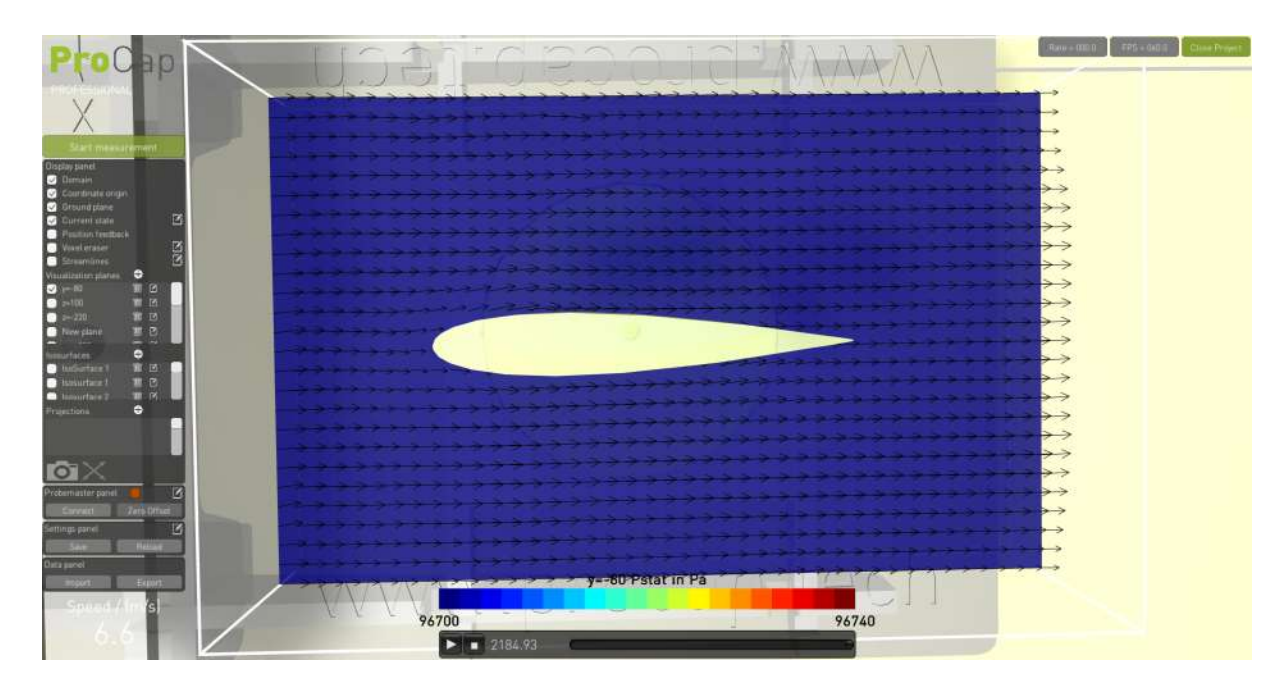


Figure 4.6: Static pressure distribution at 0° angle of attack for comparison purposes

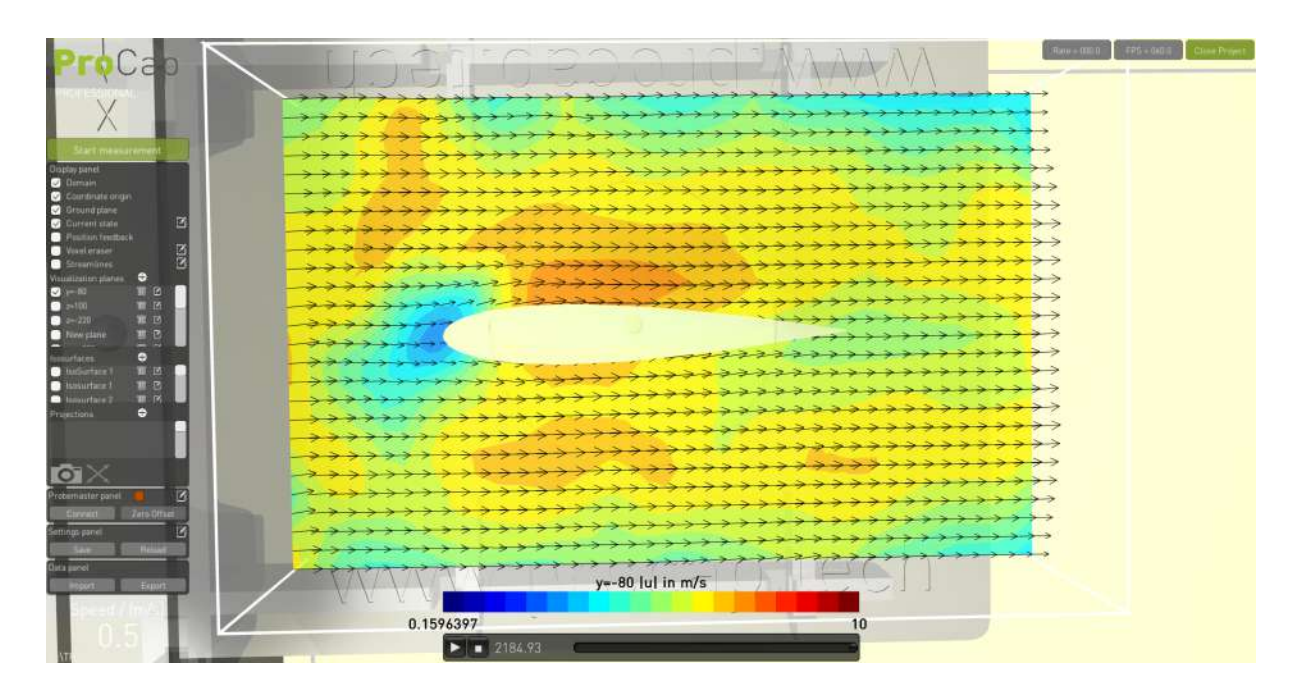


Figure 4.7: Absolute velocity distribution at 0° angle of attack

The velocity map (Figure 4.7) also shows a nearly symmetric distribution between the upper and lower surfaces, which is consistent with the static pressure data. In both figures, it is possible to observe the change in flow direction as it approaches the aerofoil, along with a noticeable reduction in speed just before the flow reaches the leading edge of the model.

4.1.2 Test 2: 5° angle of attack

By increasing the angle of attack to 5° , several significant changes can already be observed. In Figure 4.8 it can be seen that the upper region of the aerofoil experiences a lower

static pressure compared to the lower surface. This pressure difference generates an upward force, that will lift up the aerofoil.

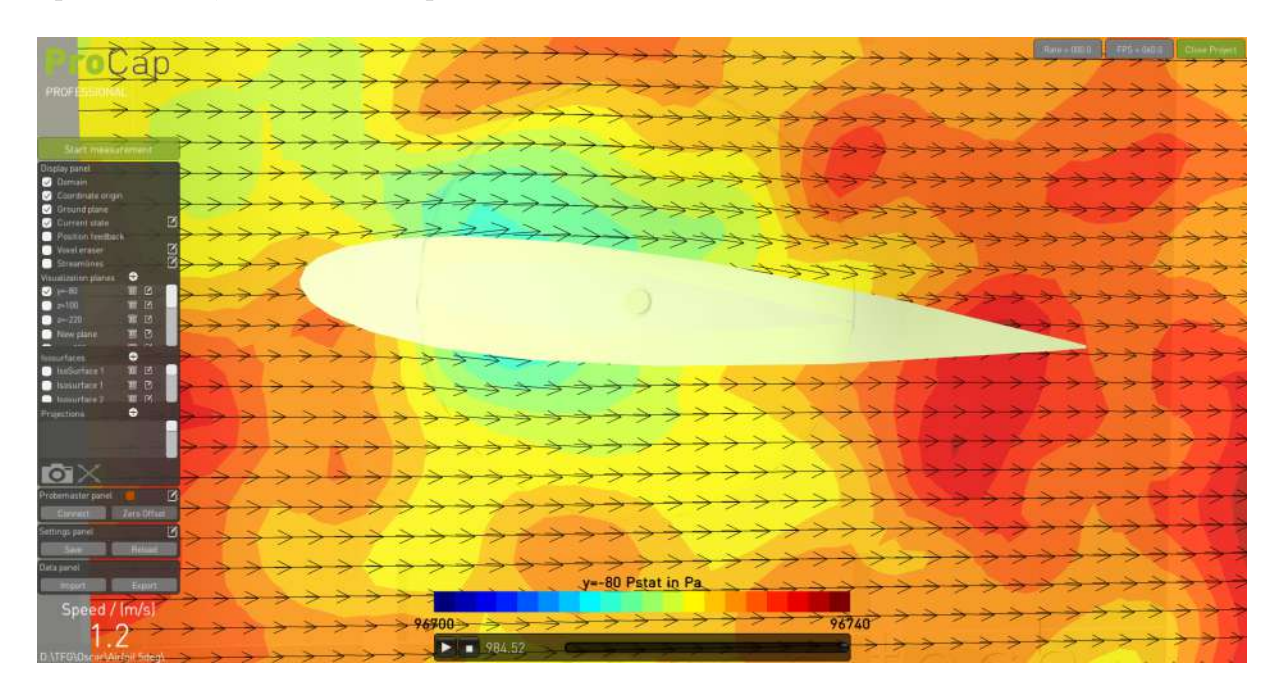


Figure 4.8: Static pressure distribution with a 5° angle of attack

The velocity maps in Figure 4.9 and Figure 4.10 show that the flow velocity increases significantly over the upper surface when compared to both the lower surface and the 0° case. According to Bernoulli's principle—assuming an ideal, inviscid, and steady flow—this increase in velocity corresponds to a decrease in static pressure on the upper surface, which contributes to the generation of lift.

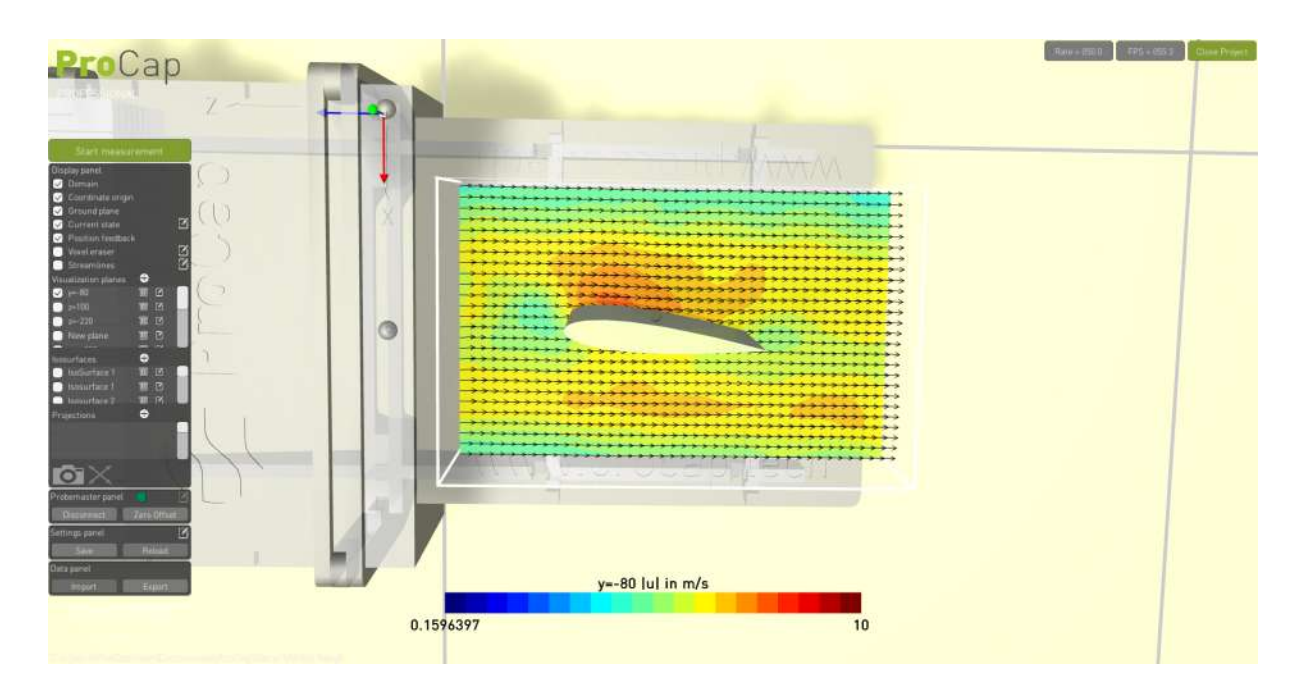


Figure 4.9: Absolute velocity distribution in the upper region with a $5\,^{\circ}$ angle of attack

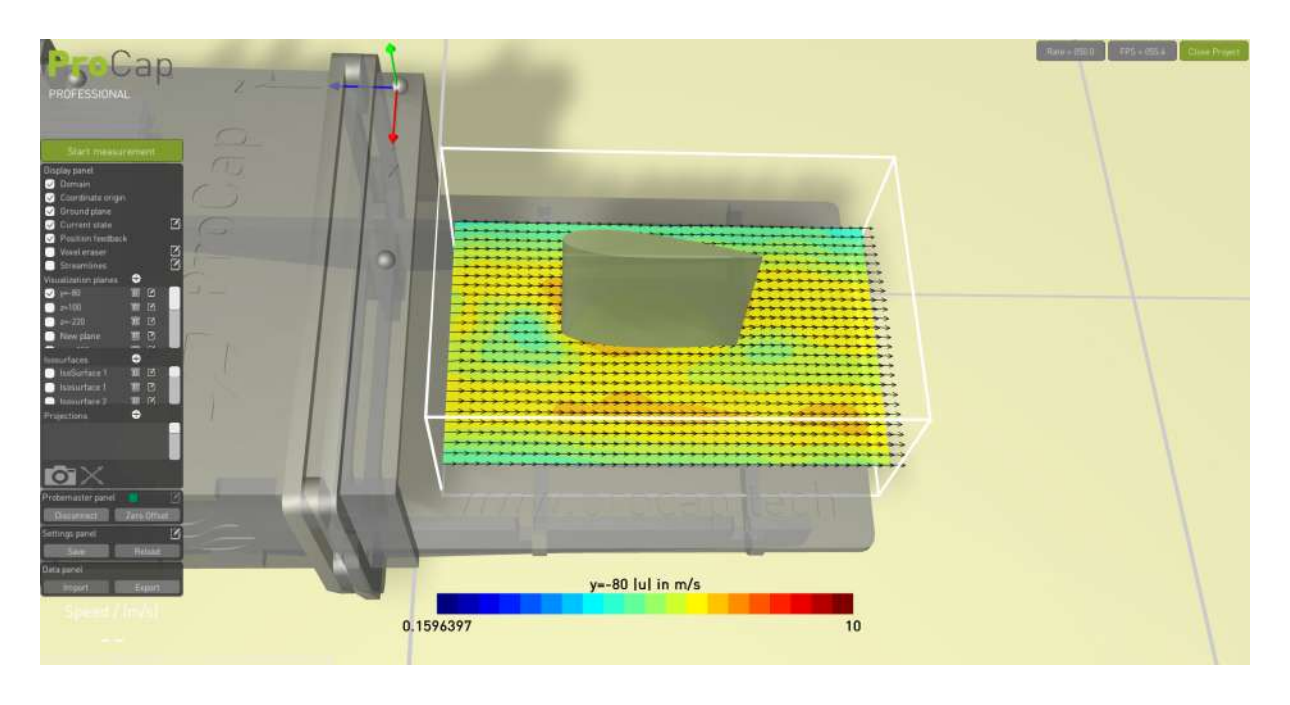


Figure 4.10: Absolute velocity distribution in the lower region with a 5 $^{\circ}$ angle of attack

4.1.3 Test 3: 10° angle of attack

For the last case, and approaching the maximum practical angle of attack, we consider a 10° angle of attack. In Figure 4.11, we can observe that the pressure over the upper surface is lower than in the previous cases, which further contributes to lift generation due to the increased pressure differential between the upper and lower surfaces.

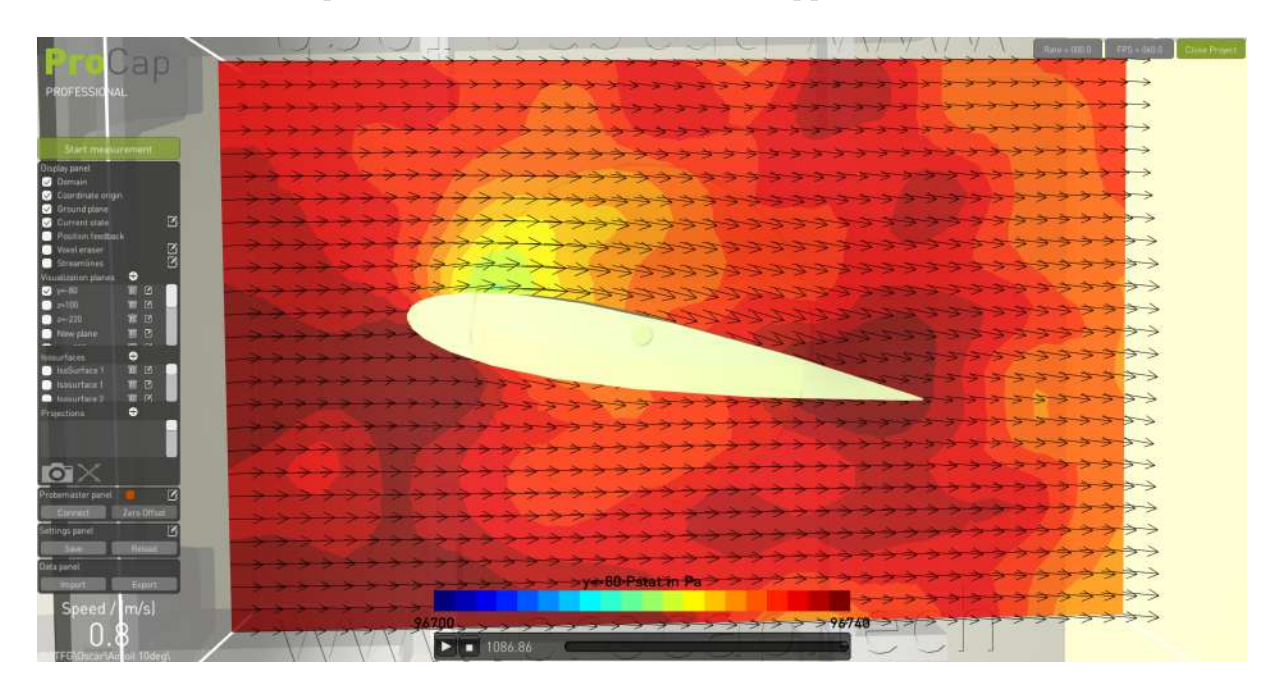


Figure 4.11: Static pressure distribution with a 10° angle of attack

A similar effect can be seen in the velocity field in Figure 4.12. The velocity magnitude over the upper surface is even greater than the previous two cases. This is consistent with Bernoulli's principle—assuming ideal flow conditions—as the increase in velocity corresponds to a further reduction in static pressure, leading to a greater lift force.

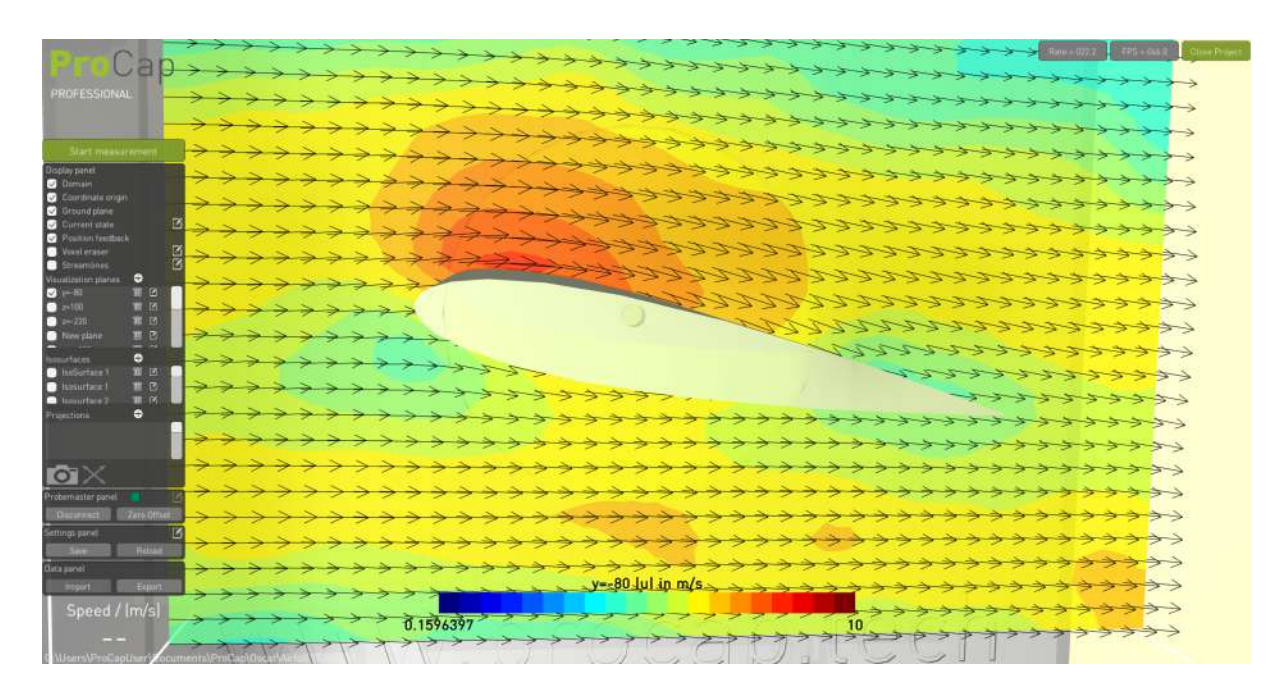


Figure 4.12: Absolute velocity distribution with a 10° angle of attack

4.2 Use case: Flow visualisation of the GTA aeroplane model

We increased the scale of the experiment and worked with the GTA model shown in Figure 4.13 (note that the targets are not used during wind tunnel testing). Due to the size of the model, testing was conducted in the large wind tunnel (Figure 4.14). The aircraft model was mounted on the universal test trolley, which allowed us to control the aircraft's pitch and, consequently, the angle of attack.

One of the most challenging aspects of the setup was the positioning of the optical camera. Ideally, the trolley should be almost entirely enclosed by the glass structure with only a small opening left for the probe, in order to maintain steady flow conditions. This setup would allow us to measure the entire aircraft model. However, this was not feasible because glass reflection interfered with the tracking of the reflective markers, and de camera's size conflicted with the enclosure mounting. Additionally, even if a suitable camera position had been found, not all the location markers would have been visible.

As a result, we had to remove half of the glass enclosure and position the optical camera on a tripod. Consequently, we were only able to measure half of the model. This setup is not ideal, as the airflow may become disturbed once it exits the wind tunnel. While this is not a critical aspect, it should be taken into account.

Using the results obtained at angles of attack of 0° , 5° , and 10° , we will analyse the wing in the same way as we did for the aerofoil. Additionally, we aim to study the wingtip vortices by placing a measurement plane just downstream of the wing.

It has to be noted that, due to time constraints, the STL model imported into ProCap is not based on a 3D scan but is instead an export from the original CAD file (e.g., a CATIA or STEP file).



Figure 4.13: GTA model with targets ${\cal G}$



Figure 4.14: Wind tunnel

4.2.1 Test 1: 0° angle of attack

In this first test, we can already observe that the static pressure on the upper surface is lower than on the lower surface. Since the aerofoil is not symmetrical, the presence of this pressure difference at a 0° angle of attack is expected. As with the aerofoil, we will use the same scale across all three test to compare the effect of varying the angle of attack.

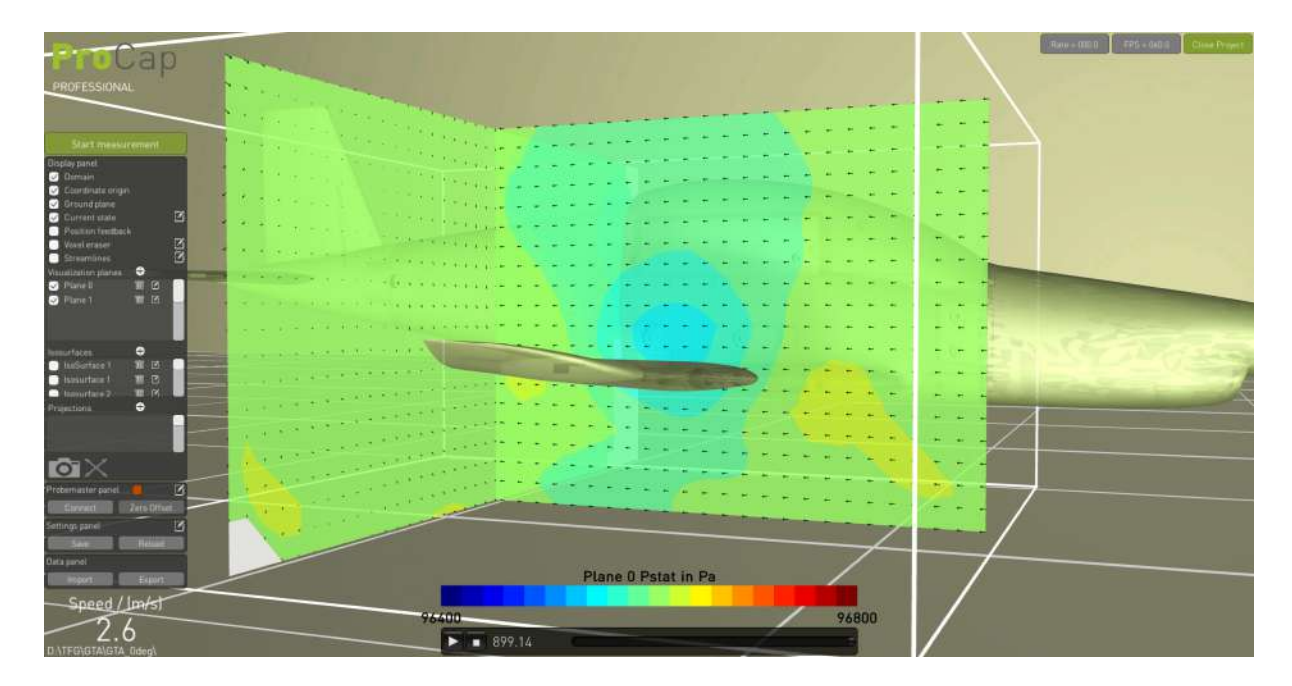


Figure 4.15: Static pressure field around the GTA model

If we now analyse the absolute velocity field (Figure 4.16) we observe that the velocity magnitude is higher above the wing and lower below it. This behaviour is consistent with Bernoulli's principle, assuming ideal flow conditions. As with the static pressure, we will use the same scale for all three cases to highlight the differences between them.

In Figure 4.17, a detailed view of the vortex formation behind the wingtip is shown. The circular pattern of the velocity vectors projected onto the plane—representing the magnitude of the absolute velocity—does not provide enough information to fully interpret this circular motion, and the arrows appear quite small. To better visualise this behaviour, we switch to the x-component of the velocity field (Figure 4.18), which is aligned with the direction of the plane. In this specific case, we also normalise the projected vectors to improve visual interpretation. We observe that x-component of the velocity is positive in the upper region (the x-axis runs from left to right, as does the velocity) and negative in the lower region (indicating flow from right to left). This distribution supports the existence of circular motion, characteristic of the wingtip vortex. Although similar effects can be observed along the span of the wing, the velocity vectors are not as clearly defined as at the tip.

In the following subsections, we will see how this phenomenon varies with the angle of attack.

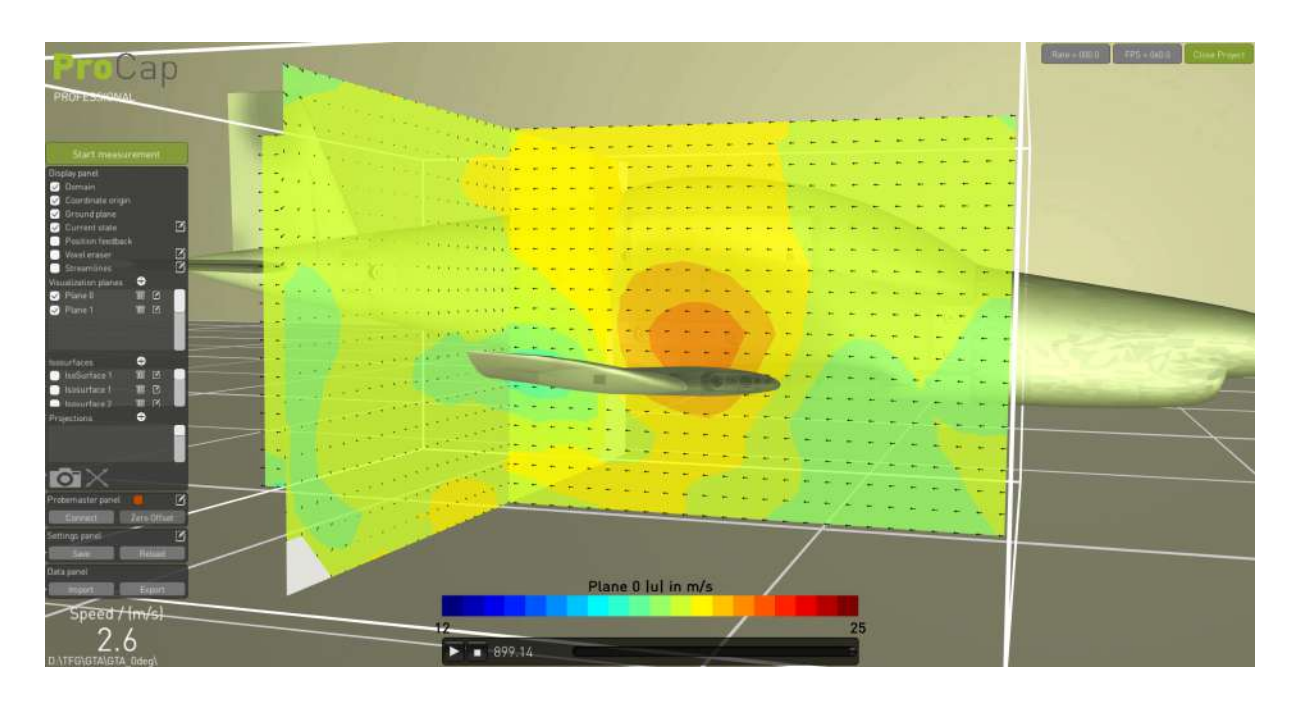


Figure 4.16: Absolute velocity distribution around the GTA model

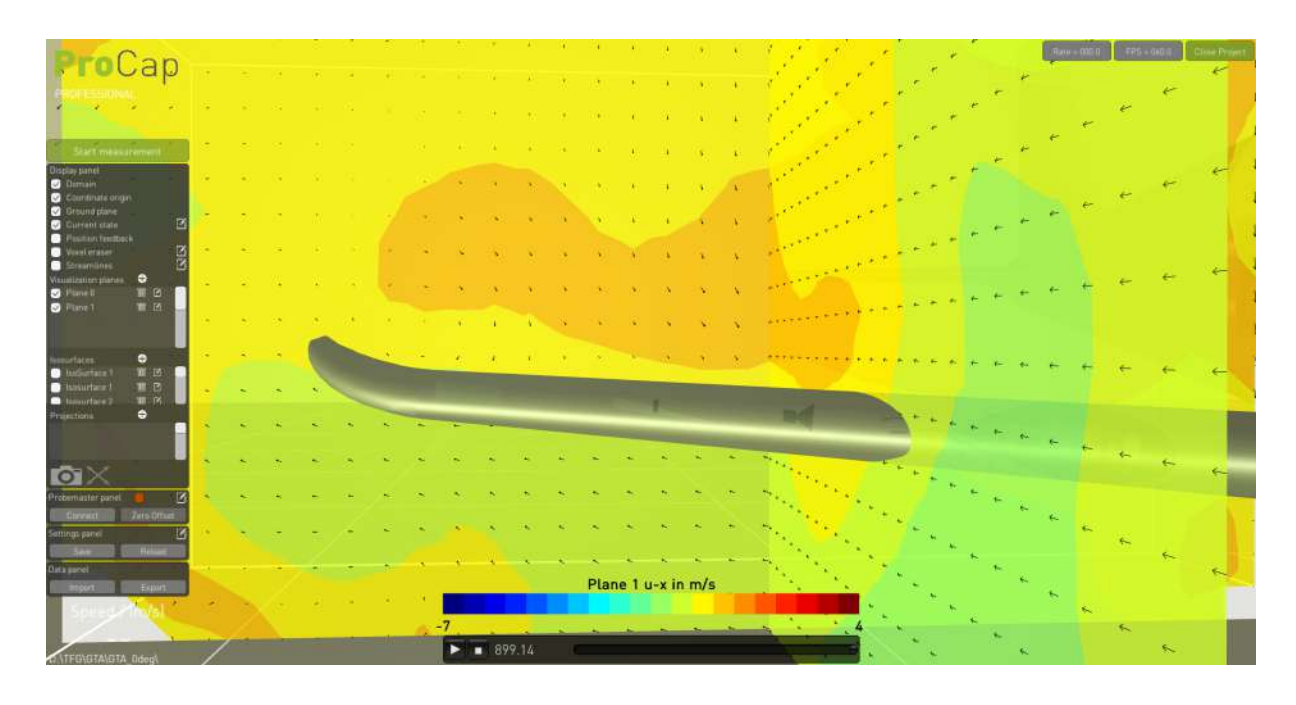


Figure 4.17: Close-up view of the vortex formation behind the wingtip

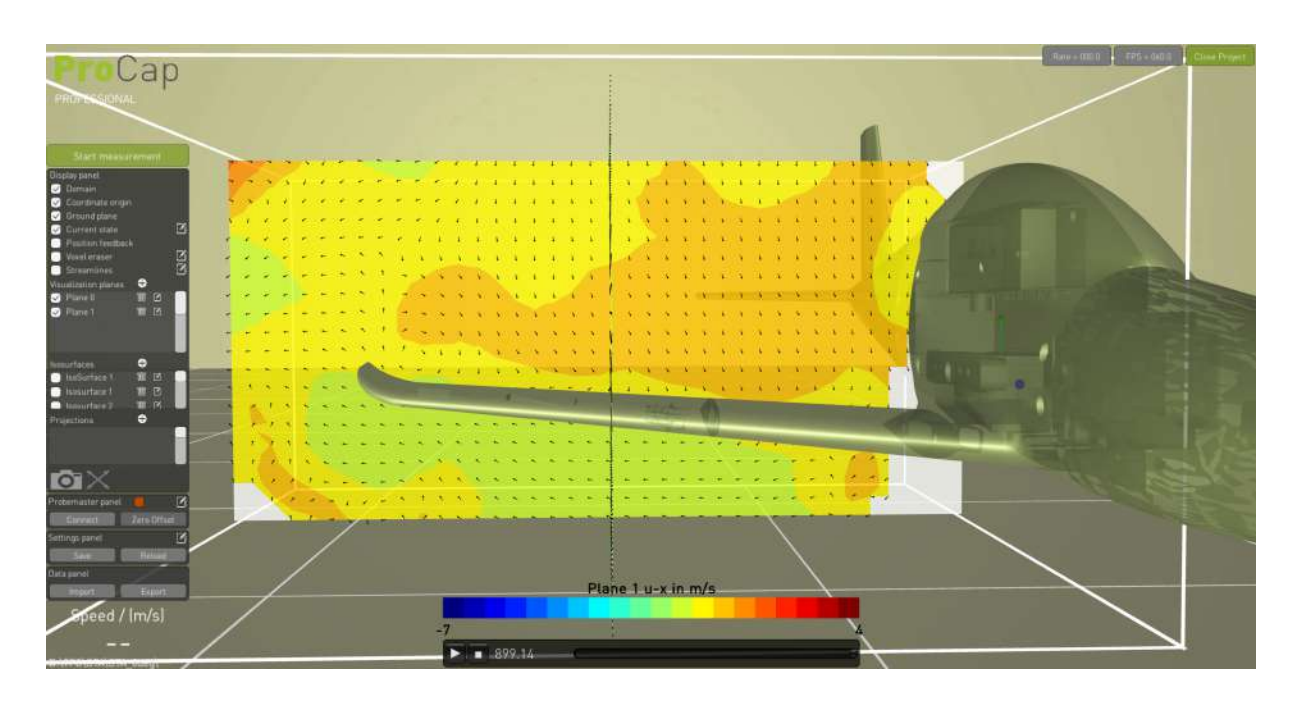


Figure 4.18: x-component of the velocity field around the GTA model

4.2.2 Test 2: 5° angle of attack

The same phenomenon observed with the aerofoil occurs here: the pressure difference increases with the angle of attack, generating greater upward lift forces. This effect is shown in Figure 4.19. The blue region above the wing is darker than in Figure 4.15, indicating lower pressure and therefore a stronger lift force.

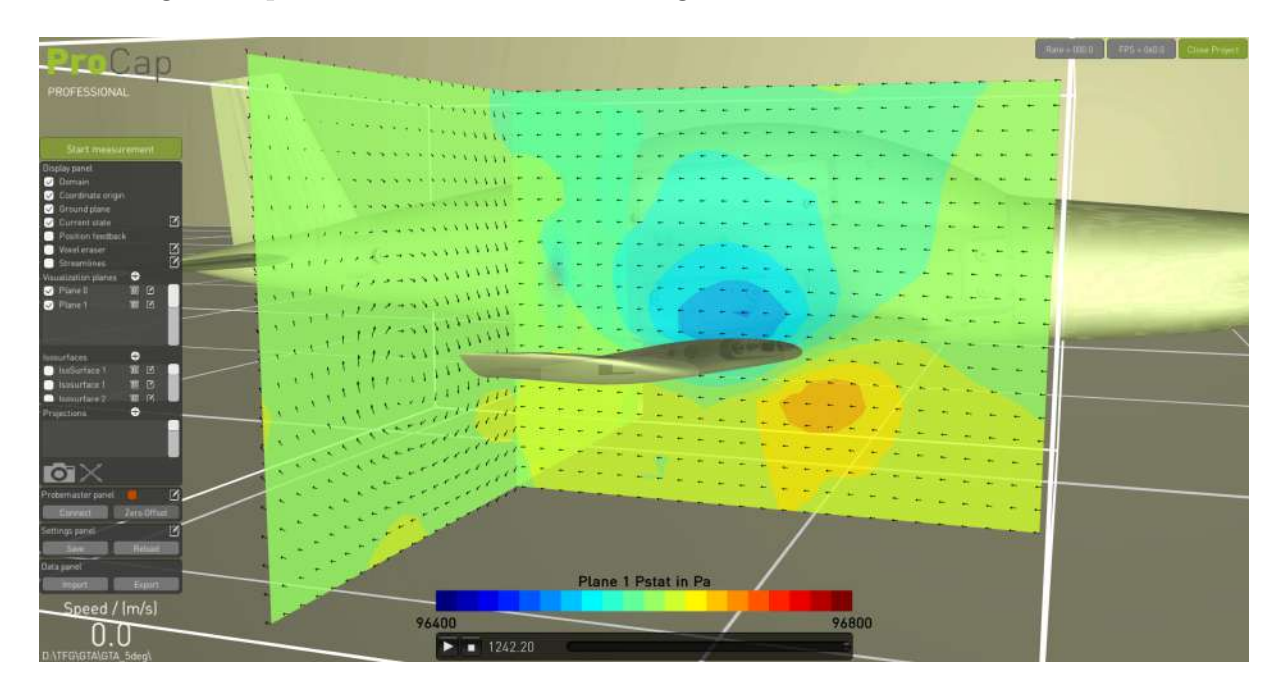


Figure 4.19: Static pressure distribution around the GTA model at 5° angle of attack

Regarding the velocity field, Figure 4.20 and Figure 4.21 show that the velocity is higher than in the case with a 0° angle of attack. One notable feature in these figures, particularly in Figure 4.21, is the presence of an unusual low-velocity region on the center-right side. This anomaly lacks a clear explanation, as it is not observed at other angles of attack.

Another important observation is the increased strength of the vortex behind the wingtip, visible in Figure 4.22. The vortex is more pronounced and contributes to an increase in drag. This goes along with the information from [40].

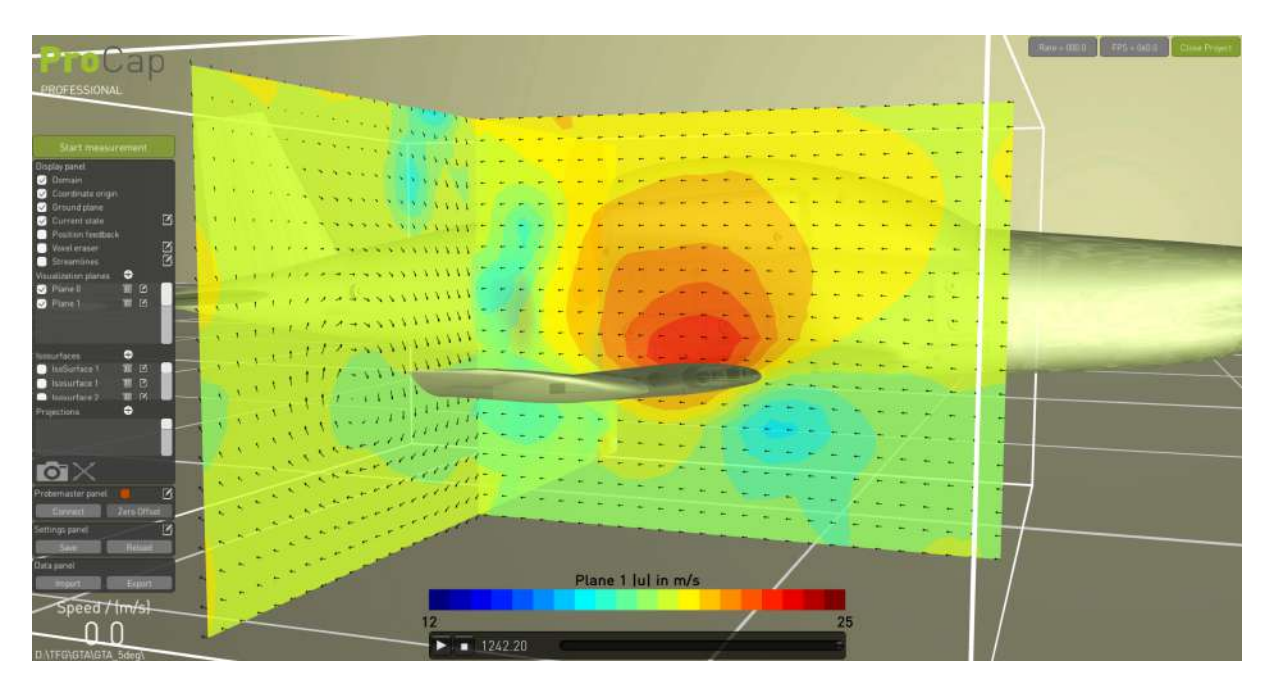


Figure 4.20: Absolute velocity distribution around the GTA model at 5 $^{\circ}$ angle of attack

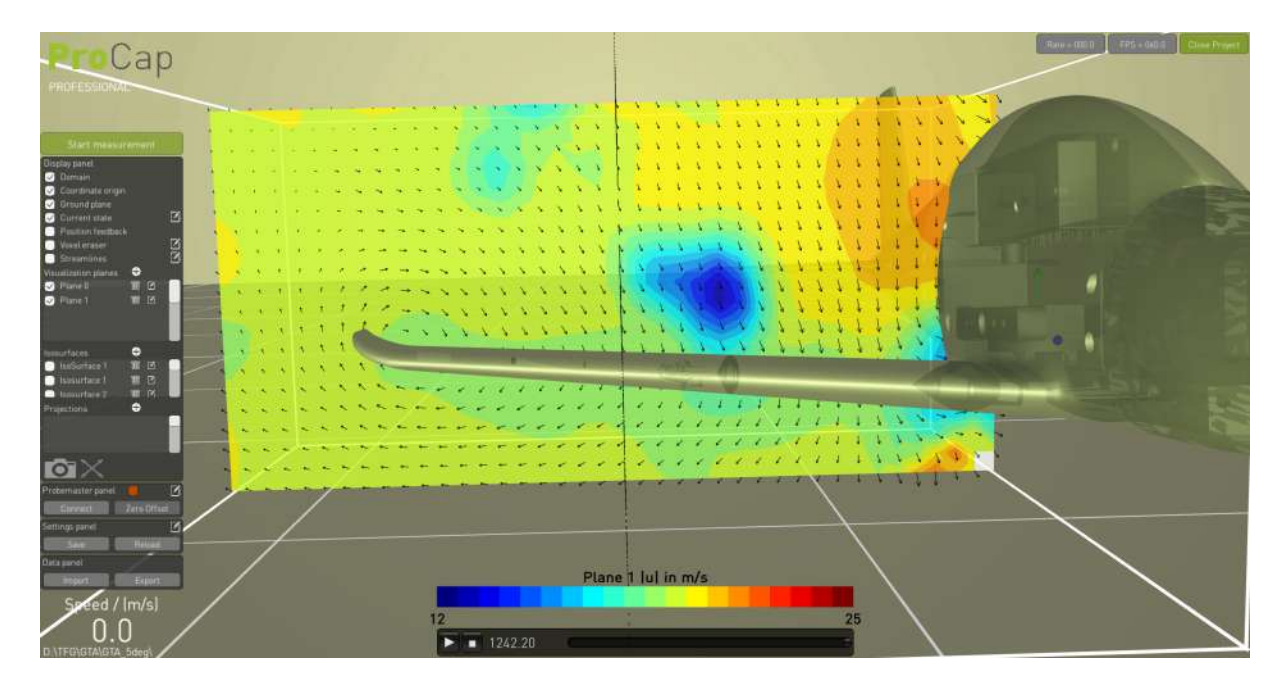


Figure 4.21: Alternative view of the absolute velocity distribution showing the low-velocity anomaly

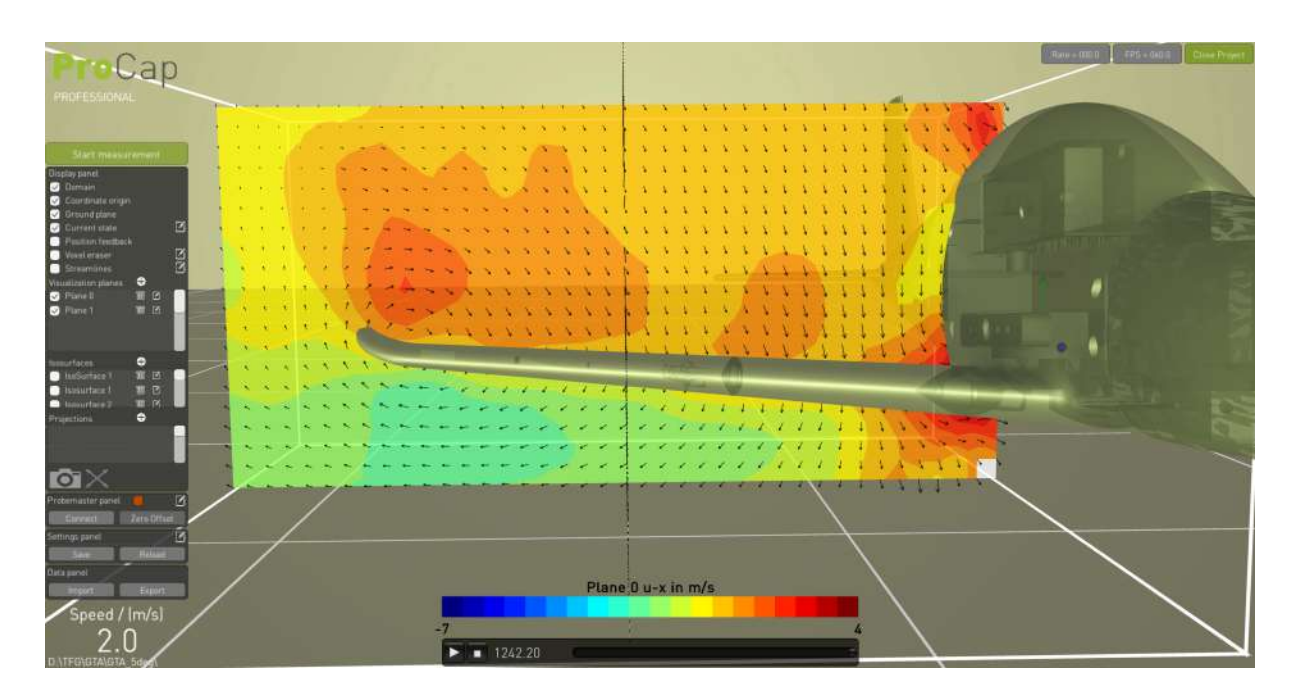


Figure 4.22: x-component of the velocity field around the GTA model at 5 $^{\circ}$ angle of attack

4.2.3 Test 3: 10° angle of attack

Finally, in this last test, we can observe that the pressure difference is even higher than in the 5° angle of attack case, as we get closer to the maximum practical angle of attack, which is around 15°. Consequently, the upper lift force is even greater than before. This difference in static pressure can be seen in Figure 4.23.

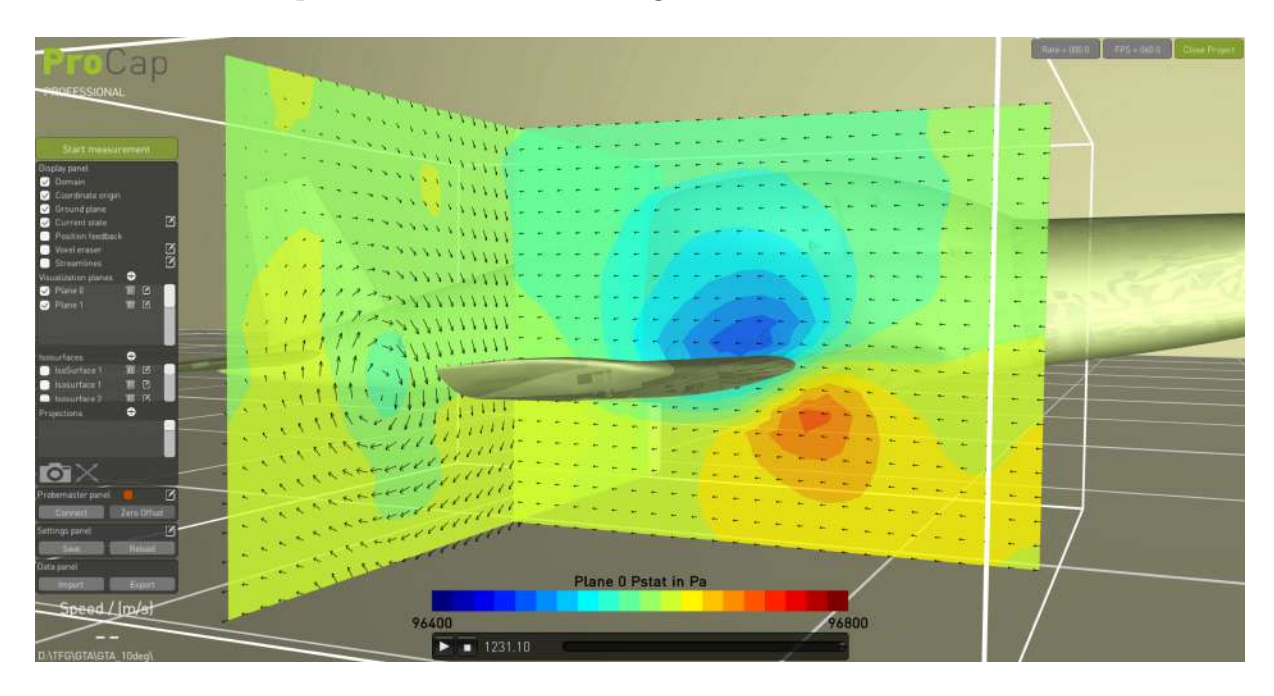


Figure 4.23: Static pressure distribution for a 10° angle of attack

As before, although the flow does not fully satisfy Bernoulli's equation due to nonideal effects, we can still use it as an approximation to understand the general inverse relationship between static pressure and velocity. This is visible in Figure 4.24. We can also observe that the vortex has increased in size. The analysis of the x-component of the velocity is carried out in the plane aligned with the x-direction (behind the wing). This alignment makes it possible to visualize how the x-component varies across the section, which helps us identify and understand the vortex structure. This is shown in Figure 4.25. As in the previous case, there is a region, this time in the upper central part, where the velocity is unexpectedly low. This anomaly lacks a clear explanation, especially considering it does not appear at other angles of attack.

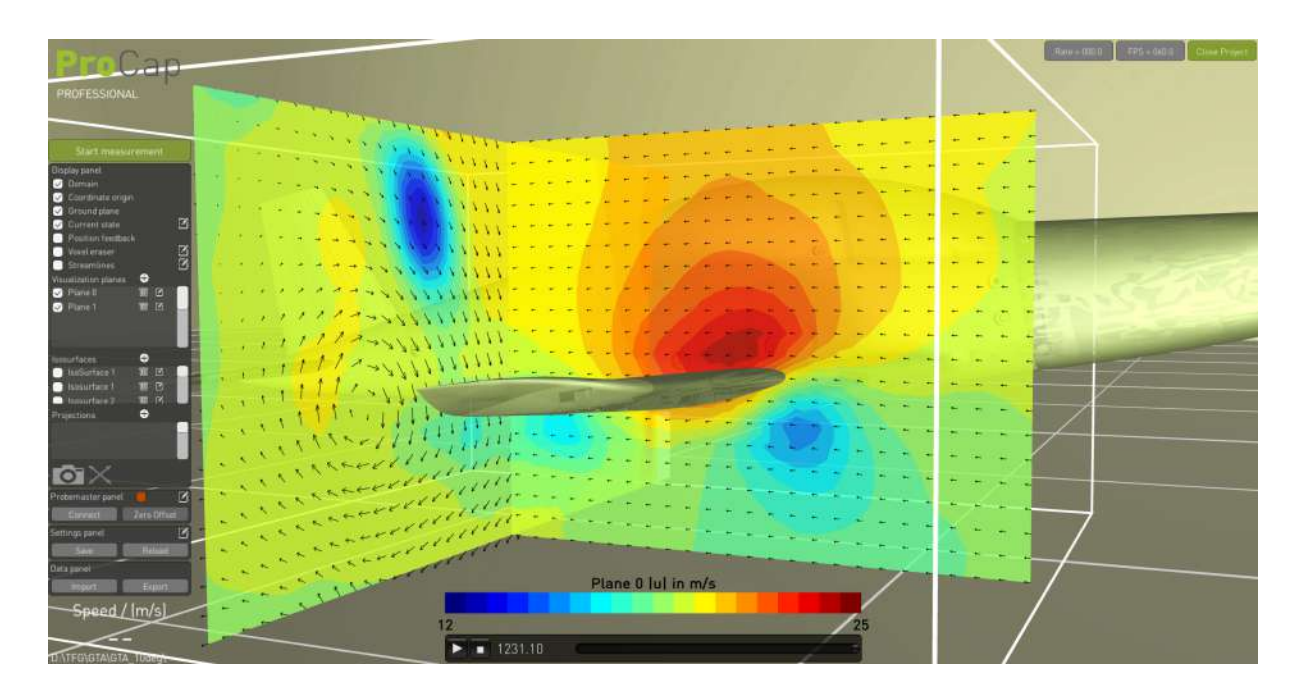


Figure 4.24: Absolute velocity distribution for a 10 $^{\circ}$ angle of attack

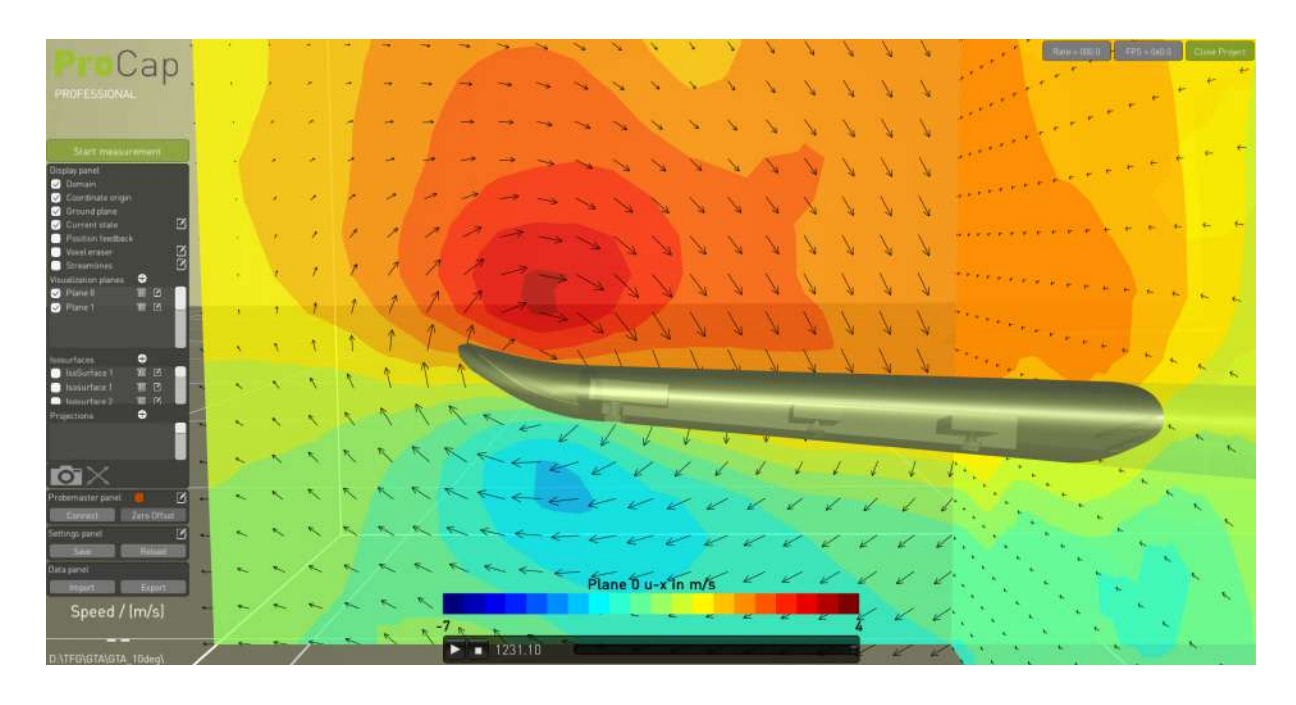


Figure 4.25: x-component of the velocity field with a detailed view of the vortex

4.3 Use case: Tolerance inspection of the GTA aeroplane model

As stated in section 3.2, we would like to check if our manufactured model meets the specified maximum wave height tolerance of $h = 0.3 \,\mathrm{mm}$. This section is divided into two subsections: the first one explains the scanning process and the second discusses how to perform the deviation analysis after having the scanned model. The following process and procedures were explained by S. Hänzi [41], from the ZHAW School of Engineering.

4.3.1 Scanning of the GTA model

For the scanning process, we used the **Creaform HandySCAN 700 600680**, a handheld red laser scanner with a volumetric accuracy of 0.06 mm, due to the medium-size scale model (about 80 cm in length). The laser offers two laser projection modes: multiple crossed lines and a single straight line. The latter provides higher precision and was used selectively in regions where the crossed lines were insufficient to define surface geometry accurately. Further technical specifications are available in appendix C.

Before starting the scan, we placed small dark and white stickers called targets on the surface of the model. They are necessary for tracking, as the scanner must always detect at least three dots to maintain spatial awareness and continuity. Targets should be positioned on flat surfaces, as they are automatically removed by the scanning software. Placing them on curved areas may cause deletion errors, potentially introducing inaccuracies.

A common challenge when scanning aerodynamic bodies, such as our model, is the presence of both very sharp edges and highly rounded surfaces. Since the targets are essential, they were placed on the wings, tail, and the flattest sections of the fuselage. Later, in the conclusions, this will be addressed again to see whether the positioning of the targets of our model had any impact on our scan or not. It is also worth noting that surface cleaning is unnecessary before scanning. The model with the applied targets is shown in Figure 4.13.

The scanning software used was **VXelements**, provided by Creaform. It allows live visualisation of the scanned surface and includes two important parameters that must be configured before scanning: the shutter speed and resolution. The shutter speed depends on the object's reflectivity (darker objects require higher shutter speeds). The resolution defines the mesh detail (triangle size in the STL file), where a compromise has to be made between file size and accuracy, as high accuracy implies high resolution but also a bigger file size. For our scan, we used a shutter speed of 4.53 ms and a resolution of 1 mm.

Once these parameters were set, the scanning commenced. During the first minutes, we confirmed that the HandSCAN 700 was adequate for our model and that neither anti-reflective powder nor a blue light scanner (which is a better option for reflective surfaces) was required.

The scanner is user friendly: pressing a single button starts the scan, while a double-click switches between laser modes.

The recommended procedure is to first scan the upper side, then the lower side of the GTA model, to minimise tracking loss. Scanning sharp features like wing leading/trailing edges and the tail required switching to the single-line laser mode and scanning repeatedly, as it was difficult for the scanner to recreate them.

After completing the upper side, residual scan artefacts were removed in VXelements by inverting the plane selection. The model was then flipped, supported with a targetcovered box (Figure 4.27), and scanned from below. It is really important to make sure that the scanner did not capture the connection between the box and the aeroplane, as this would complicate post-processing. Also, any movement of the plane during scanning could cause loss of tracking and alignment. We had to start the scanning process first using known nodes from the upper side to ensure the surface continuity in the lower side.

In both sides of the aeroplane the scanner had some difficulties with the semi-transparent wingtips and the dark plastic tail.

Once the entire scanning process was completed, the entire model could be visualised. Some misalignment was observed at the trailing edge of one wing, likely due to the scanner's limitations with sharp features and the challenge of merging top and bottom scans in those areas.

VXelements also allows localised refinement of the mesh by reducing triangle size (thus increasing the accuracy) in selected regions. This is done by selecting a region and increasing the resolution by lowering the triangles size (for instance, from 1 mm to 0.5 mm). Finally, we exported the STL file of the complete GTA model in two versions: one with 1 mm resolution another with 0.4 mm resolution.

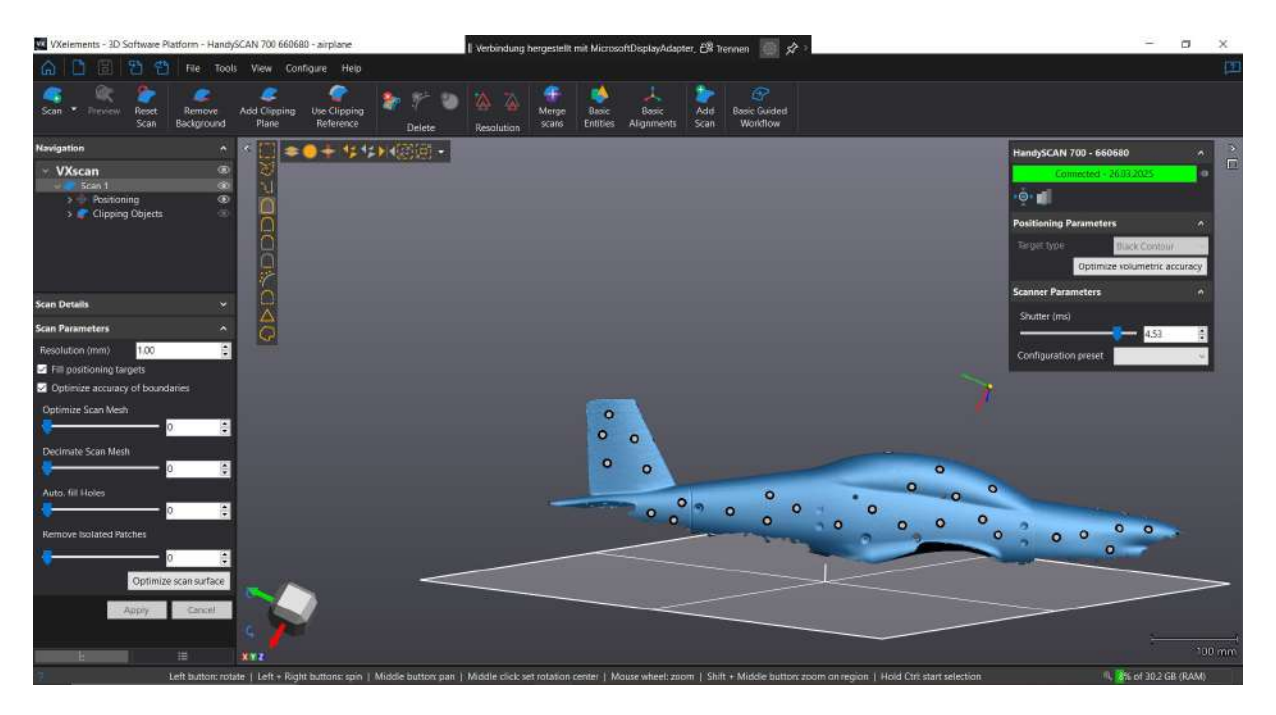


Figure 4.26: Interface of VXelements and visualisation of the scan

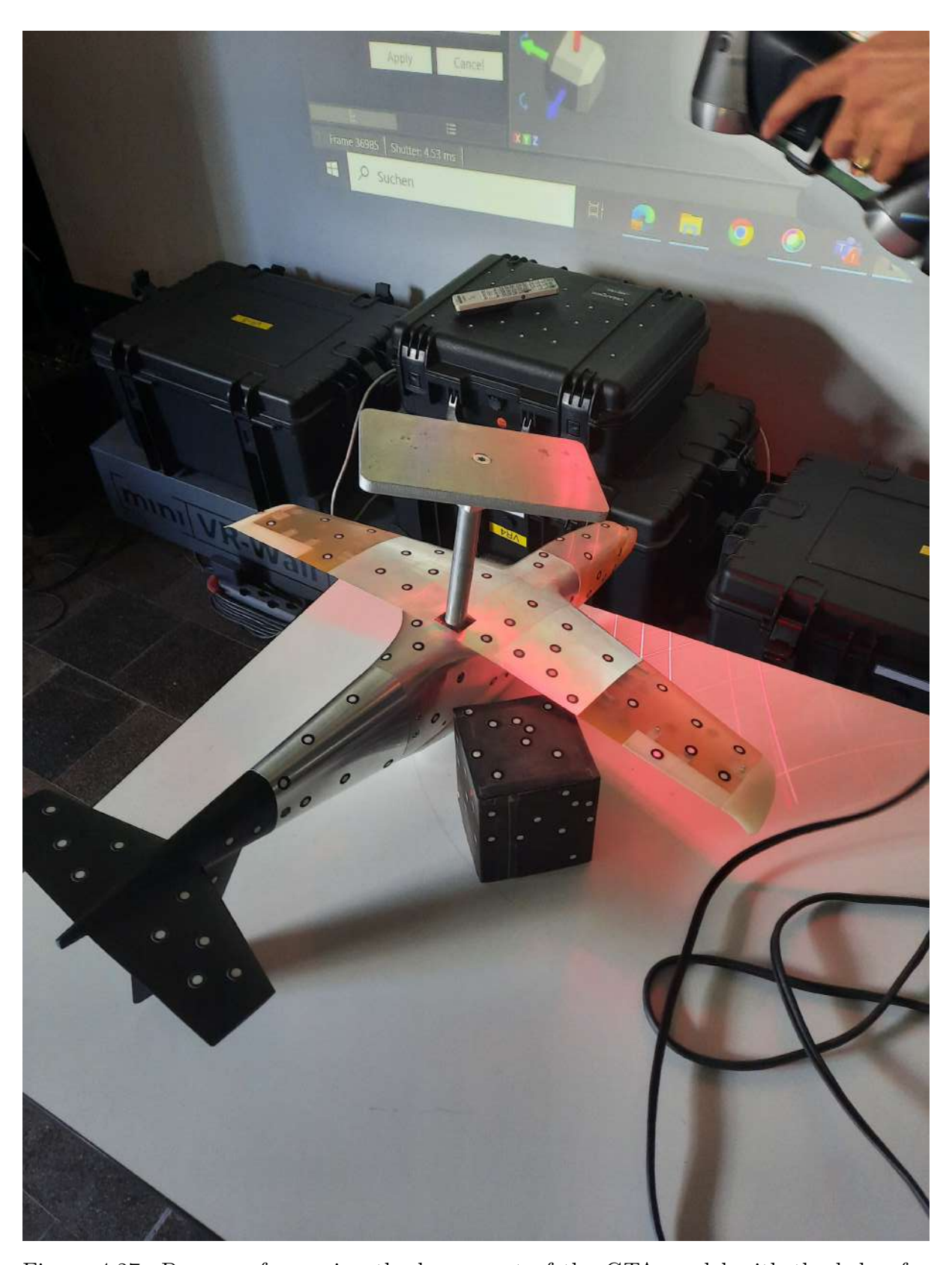


Figure 4.27: Process of scanning the lower part of the GTA model with the help of a targeted box $\frac{1}{2}$

4.3.2 Tolerance analysis

Once we had the STL file from the 3D scan, we imported it into **3DEXPERIENCE**. In this software we compared the STL file with the original CAD model (provided as a STEP (STP) file).

First, it was necessary to import both the CAD model and the STL file (Figure 4.28). In our case, the CAD model consisted of two independent sections, almost split along the symmetry axis of the aeroplane. We had to merge and assemble these sections into a single part so that we could extract the entire surface and compare it with the scan. The position of the model within the software was not an issue, as the model and the scan were unified for the comparison. Once we obtained a single object (referred to as Join.1 in Figure 4.29) we created a geometrical set in which we imported the 3D scan. The scan was imported via the "Digitalisation Part" function. Note: although the screenshots in Figure 4.28 and Figure 4.29 indicated a resolution of 0.04 mm (the triangle side length), the actual resolution was 0.4 mm. It is a naming error.

One important setting before importing the STL was the scale factor. In our case, the scale was set to 1 (in millimetres), since both models used the same units and scale.

The next step was to align the scanned mesh with the CAD model. Since we did not have any flat or primitive geometry to use as a reference or constraint for alignment, we used a fast alignment tool called "Best Fit". In this tool, we specified the STL and the CAD model as the reference. This tool allowed the software to align the models automatically. The result is shown in Figure 4.29. While the alignment was not bad, it was insufficient for accurate comparison, as the two models were visibly separated.

From this point on, we worked with the 1 mm STL file instead of the $0.4 \,\mathrm{mm}$ one, due to time constraints and the need for faster alignment procedures. The process was analogous as with the $0.4 \,\mathrm{mm}$ resolution. The "Best Fit" alignment result for the $1 \,\mathrm{mm}$ resolution was visually identical to that of the $0.4 \,\mathrm{mm}$ scan.

The next alignment step was "Fine Tuning", since the scan was already very close to the CAD geometry. The result is shown in Figure 4.30. In this case, we saw a mixture of two colours in most regions. 3DEXPERIENCE did not know which surface to prioritise as both fitted together really good. In contrast, when only one color was visible (as in Figure 4.29), it suggested that one part dominated or was misaligned with respect to the other. At this point we were ready to perform the deviation analysis. To do this, we clicked on the "Deviation Analysis" button and selected the CAD model as the reference and the STL file as the mesh to be analysed. The result is shown in Figure 5.2.

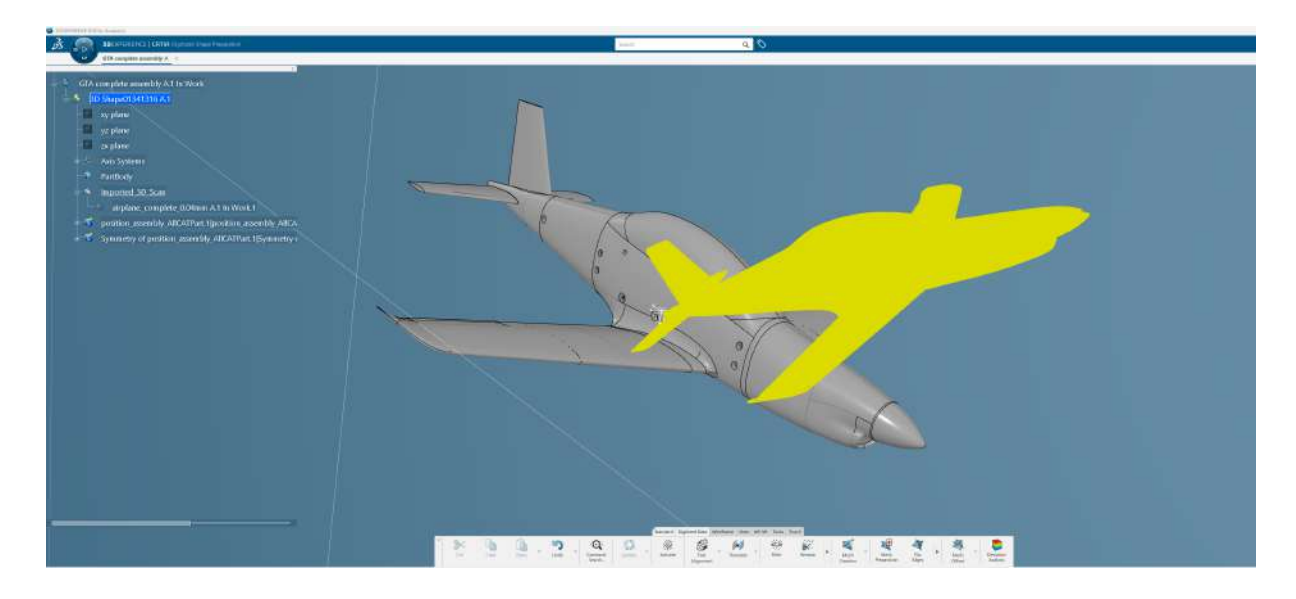


Figure 4.28: Interface visualisation of 3DEXPERIENCE with the original and the scanned model (in yellow) $\frac{1}{2}$



Figure 4.29: Best Fit alignment

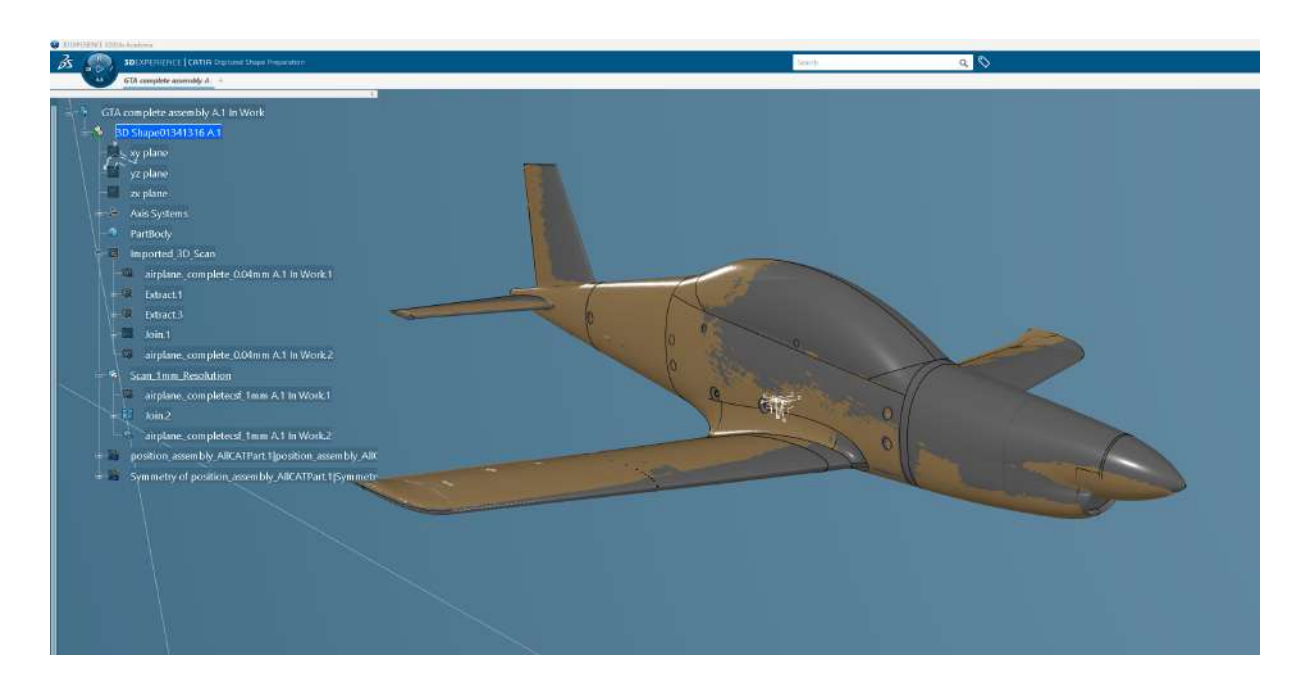


Figure 4.30: Model and scan after the fine tuning alignment

Chapter 5

Discussion of results

5.1 Use case: Flow visualisation of the aerofoil model

In all three cases, we observed that the angle of attack has a significant impact on the flow behaviour. In the first case, both the upper and lower regions showed a similar distribution of pressure and velocity, as the aerofoil has a symmetrical profile. In the remaining two cases, static pressure decreased and velocity increased as the angle of attack grew.

One of the first considerations should be the positioning of the axis in the CAD model. Ideally, it should be located along the center axis of the body. In our case, however, it was defined at the leading edge of the aerofoil, just above the circular base, which caused some issues when positioning the model within ProCap.

It is also important to note that ProCap is not precise enough for highly accurate calculations. For example, regions near the leading edge displayed a wider low-velocity area than would be expected in more precise simulations, where the flow separation towards the upper and lower surfaces of the aerofoil should be smaller. In some cases, this region also appeared slightly misaligned with the model due to positioning errors of the optical probe.

Another limitation is that ProCap does not allow the detection of the boundary layer separation and the formation of vortices near the trailing edge.

Additionally, data collected very close to the model's surface may lack accuracy. As explained in section 2.5.2, proximity to the wall introduces some measurement challenges. Since the calibration process for the iProbe is not fully detailed in the manual, which only mentions that calibration is stored in the probe head, we cannot confirm whether the wall effects were taken into consideration during calibration.

Nevertheless, the ProCap software clearly offers strong educational value. In addition to visualising flow planes, it also allows the visualisation of streamlines defined between two points, which helps to better understand the flow behaviour.

5.2 Use case: Flow visualisation of the GTA model

In this use case, we explored the effect of varying the angle of attack using a larger model in the big wind tunnel. Most conclusions are similar to those from the previous case. For instance, boundary layer separation cannot be visualised in the wing's cross-sectional plane; the software is not precise enough to provide highly accurate information (at least as displayed within the program, though the data can be exported and processed in other

tools); and small alignment errors may occur. However, there are additional points to consider:

- It is not possible to measure both sides of the entire aeroplane model due to its size and limited field of view of the camera setup, as the three optical cameras are fixed together and cannot be moved independently.
- The camera is very sensitive to reflections, which creates issues when detecting the reflective markers in *Motive:Tracker*. If a reflection appears in some part of the plane where tracking is needed with the probe, there is no way to mask it, so a different tracking location must be selected.
- The position and orientation of the reference reflective markers must also be carefully considered, as the model needs to be correctly centred in *Motive:Tracker* to ensure a good positioning and measurement in ProCap.
- We had to leave the universal trolley with the GTA model open for the reasons mentioned above. This can affect the measurement, as the flow might disperse after exiting the wind tunnel. As noted in section 4.2, this is not critical, but it must be taken into account.
- The region near the fuselage behind the wing of the aeroplane was not measured, as the stick holding the model would have interfered with the flow analysis. We avoided this because it introduces an effect not present in real life applications.
- Some regions showed unusual results where data was not properly acquired, without a clear explanation. These are the blue regions in the velocity figures shown in the different subsections of section 4.2.
- When comparing different experiments using the same scale, it is often difficult to establish a common scale across all cases. To visualise detailed pressure or velocity information, the colour scale must be adjusted, but the chosen scale might not be appropriate for the rest of the cases. As a result, when comparing experiments, some information will be lost.
- A positive aspect is its ability to visualise abstract concepts in a very interactive and intuitive way. It might not be suitable for very precise calculations, but it serves well as a teaching tool. Moreover, ProCap enables the visualisation of simple streamlines from the obtained data (Figure 5.1), which helps to better understand the concepts. The only major limitation is that the analysis is restricted to certain predefined planes and does not cover the entire control volume.

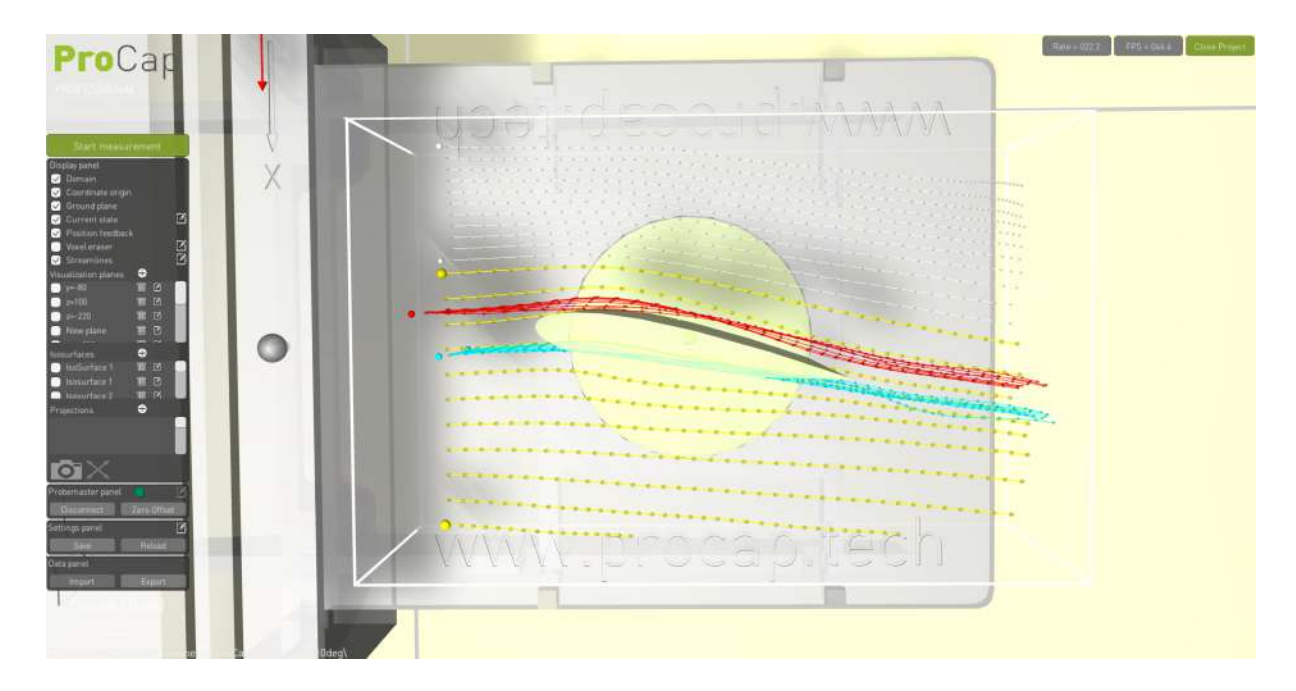


Figure 5.1: Streamline visualisation in ProCap

5.3 Use case: Tolerance inspection of the GTA aeroplane model

Figure 5.2 shows the deviation analysis between the original CAD model and the scanned geometry to assess whether the tolerance requirements are met. In this case, it is not possible to draw a definite conclusion, as the analysis does not provide conclusive results due to the following reasons:

- There is a mismatch in the scan data between the upper and the lower parts, especially at the wing's trailing edge, as mentioned in section 4.3.1.
- Due to time constraints we were not able to work with the 0.4 mm resolution scan file. A higher resolution (with smaller triangles) would allow for better representation of sharp edges, as the mesh can adapt better to the curvature (you cannot do it with big triangles). This could explain the large deviations observed in very sharp-edged regions. However, it does not explain the significant deviations found in relatively flat areas like the upper surface of the wing. Therefore, this factor alone cannot explain the observed results.
- The alignment was performed using the "Best fit" method without any constraints. The limitation of this approach is that it gives full control of the alignment to the software, which may not produce optimal results for our specific comparison.
- We can also discard the possibility that the lack of conclusions is due to the placement of targets in high-curvature regions. If this were the case, circular bumps would appear in the deviation analysis at those locations. However, such bumps are not present where the targets were placed.
- The material difference between the two main parts of the model, aluminium EN AW-7075 and an unspecified polymer, does not fully explain the deviations either.

For instance, one wing tip from polymer shows large deviations, whereas the opposite wing tip, also made from polymer, remains well within the imposed tolerance of $h = 0.3 \,\mathrm{mm}$ stated in section 3.2.

• The dark polymer used for the tail does not allow for any clear conclusion either. The deviation at the connection between the tail and the aluminium body is high, while the aluminium part remain low within the tolerance. Moreover, some leading edges of the tail wings show high deviations, whereas others are inside the acceptable limits. Therefore, we cannot state any conclusion.

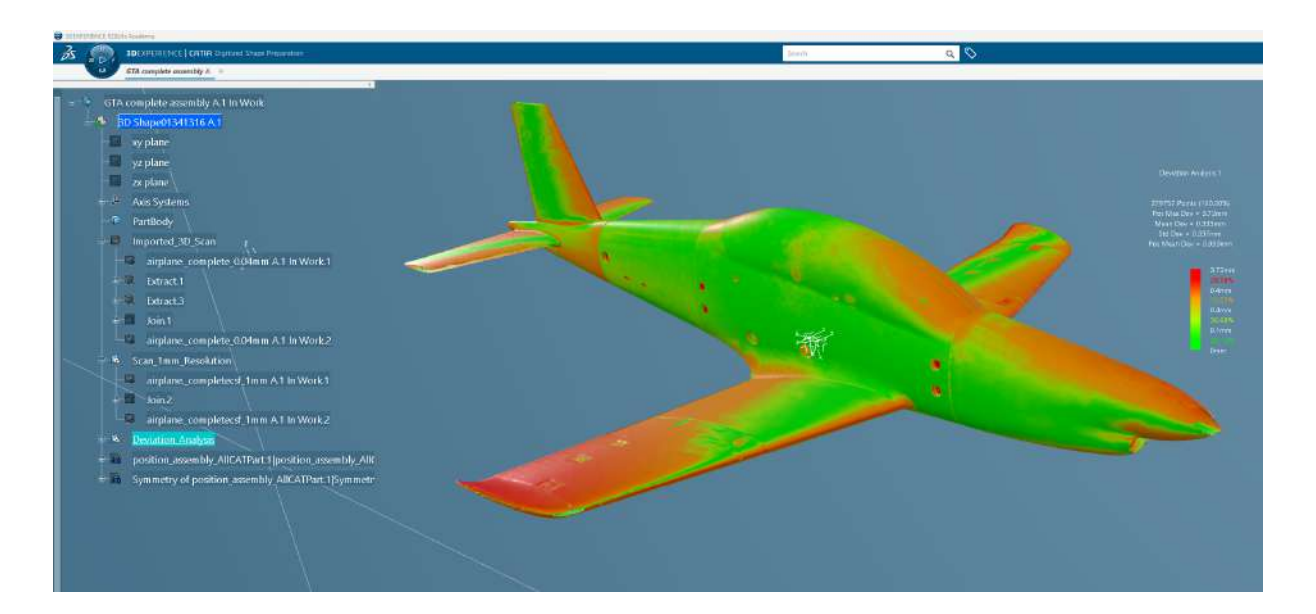


Figure 5.2: Deviation analysis of the GTA model

Chapter 6

Conclusion

Throughout this thesis, we have explored the significant role of 3D scanning in aerodynamics, along with the capabilities of the ProCap system, which allows for the integration of a 3D scanned model with a real-time visualisation of aerodynamic tests.

Regarding ProCap, we can conclude that it is an easy-to-use software with very interactive features, perfect for teaching purposes. This software works by importing STL files, so in case the original CAD is unavailable, any scanner capable of directly generating STL files can be used, with no need for post-processing. In our case, due to time constraints, we were not able to use the 3D-scanned model, and instead exported the STL file directly from the original CAD. This was not a major issue, as it is only intended for visualisation within ProCap and did not have any technical significance. However, ProCap is not without limitations, such as a lack of accuracy, slight misalignments between the measurement data and the model, the restriction to predefined planes for visualisation, and the challenges related to the optical camera and its great sensitivity to reflections. These findings could likely be extended to other similar measuring software.

Future work could focus on evaluating the software's actual precision, and how it takes into account the wall-effect. Alternative tracking methods for the probe could also be investigated to mitigate reflection-related problems, especially as most aerodynamic bodies are highly reflective. Potential alternatives include acoustics systems or artificial intelligence-based tracking solutions.

As for the 3D scan and the tolerance inspection, the obtained results demonstrate the great potential of 3D scanners in accurately recreating real-world surfaces. However, they are not particularly effective at capturing very sharp edges, as targets cannot be placed in high-curvature regions. Further research could define the optimal triangle size (the resolution) needed to accurately represent sharp edges, as we have seen that large-size triangles do not allow for sufficient detail in such regions.

Additionally, a more in-depth study is required to draw meaningful conclusions from the deviation analysis, which was not achieved in this thesis. A good starting point would be to examine the 0.4 mm resolution scan to see whether it improves results. If it still fails to provide any useful information, other strategies could be explored. One approach is to look for possible ways to set restrictions to the scanned STL file. In our case we used "Best Fit" and "Fine Tuning" alignment options, which delegate the task of making the alignment entirely to the software. Another method, used in a separate project, involved creating a real-world coordinate axis in the same position in both the CAD and the physical object to be scanned. This enabled the creation of a primitive line in the scanned mesh, which could be constrained and aligned with the defined axis in the CAD

software. A further area of research would be to identify where such restrictive primitive geometries could be located on the aeroplane's scanned model, which typically lack clear reference shapes. Another important aspect is determining the direction of the deviation, as 3DEXPERIENCE only provides the absolute value. This direction provides valuable information to know whether the data is misaligned or if it meets the requirements.

Bibliography

- [1] R. H. Helle and H. G. Lemu, "A case study on use of 3d scanning for reverse engineering and quality control," *Journal of Manufacturing Processes*, vol. 43, pp. 189–197, 2019. DOI: 10.1016/j.jmapro.2019.06.025.
- [2] M. A.-B. Ebrahim, "3d laser scanners' techniques overview," *International Journal of Science and Research (IJSR)*, vol. 4, no. 10, pp. 323-331, Oct. 2015, Accessed: 22-abr-2025. [Online]. Available: https://www.researchgate.net/publication/282753883_3D_Laser_Scanners%27_Techniques_Overview.
- [3] S. M. A. S. Shadman Tajwar Shahid and M. H. K. Bhuiyan, "Automatic contact-based 3d scanning using articulated robotic arm," arXiv preprint arXiv:2411.07047, Nov. 2024, Accessed: 01-Jun-2025. [Online]. Available: https://arxiv.org/pdf/2411.07047v1.
- [4] Keyence Corporation. "3d scanner." Accessed: 01-Jun-2025. [Online]. Available: https://www.keyence.com/products/3d-measure/3d-scanner/.
- [5] M. Kupiec, "Coordinate measurement systems cmm and cma-characteristic and methods of their accuracy evaluation," *Astronomical Journal*, vol. 143, p. 109, 2012, Accessed: 01-Jun-2025. [Online]. Available: https://www.astrj.com/pdf-143-109?filename=COORDIANATE%20MEASURMENT.pdf.
- [6] 3. S. (Ltd, Contact scanning/probing, https://3dscanners.co.uk/services/contact-scanning-probing/, Accessed: 22-abr-2025, 2025.
- [7] G. 3D, 3d scanning, Accessed: 22-abr-2025, 2025. [Online]. Available: https://gamma3d.co.uk/3d-scanning/.
- [8] K. Olsson and T. Persson, "Shape from silhouette scanner creating a digital 3d model of a real object by analyzing photos from multiple views," Performed at VCG (Visual Computing Group), CNR (Italian National Research Council), Pisa, Italy. Examiner: Prof. Anders Ynnerman. Tutor: Dr. Claudio Montani, M.S. thesis, Linköping University, Sweden, Jan. 2002. [Online]. Available: https://www.diva-portal.org/smash/get/diva2:18671/FULLTEXT01.pdf.
- [9] Eisko. "What is the best 3d scanning technology for film productions?" Accessed: 22-abr-2025. [Online]. Available: https://eisko.com/2023/02/17/best-3d-scanning-technology/.
- [10] V. Koneva. "What is laser 3d scanning?" Accessed: 23-abr-2025. [Online]. Available: https://www.artec3d.com/learning-center/laser-3d-scanning.
- [11] AVSystem. "Tof: Time-of-flight overview, principles, advantages." Accessed: 23-abr-2025. [Online]. Available: https://avsystem.com/blog/linkyfi/time-of-flight.

- [12] HWYL. "Time of flight 3d camera: What you need to know." Accessed: 23-Apr-2025. [Online]. Available: https://hwyl.in/time-of-flight-3d-camera/.
- [13] FRAMOS. "Advantages and disadvantages of time-of-flight cameras." Accessed: 23-Apr-2025. [Online]. Available: https://www.framos.com/en/articles/advantages-and-disadvantages-of-time-of-flight-cameras.
- [14] A.-B. Mostafa and M. Ebrahim, "3d laser scanners' techniques overview," *International Journal of Science and Research (IJSR)*, vol. 4, pp. 5–611, Oct. 2015.
- [15] O. Engineering. "Time-of-flight vs. phase-based laser scanning." Accessed: 2025-03-14. [Online]. Available: https://www.ohare-eng.co.uk/blog/tof-vs-phase-based.
- [16] Hermary. "Principles of laser triangulation." Accessed: 23-Apr-2025. [Online]. Available: https://hermary.com/learning/principles-of-laser-triangulation/.
- [17] V. Marcune and S. Iles. "Understanding surface roughness." Accessed: 27-Apr-2025. [Online]. Available: https://www.edmundoptics.com/knowledge-center/application-notes/optics/understanding-surface-roughness/.
- [18] I. O. for Standardization (ISO), En iso 1101: Geometrical product specifications (gps) geometrical tolerancing tolerances of form, orientation, location and run-out, Accessed: 27-Apr-2025, European Committee for Standardization (CEN), 2017.
- [19] I. O. for Standardization (ISO), En iso 4287: Geometrical product specifications (gps) surface texture: Profile method terms, definitions and surface texture parameters (iso 4287:1997), Accessed: 27-Apr-2025, European Committee for Standardization (CEN), Aug. 1998.
- [20] I. O. for Standardization (ISO), En iso 25178-2: Geometrical product specifications (gps) surface texture: Areal part 2: Terms, definitions and surface texture parameters (iso 25178-2:2021), Accessed: 23-Apr-2025, European Committee for Standardization (CEN), Jan. 2022.
- [21] Y. Lin, S. Raghunathan, B. Raghunathan, and S. McIlwain, "Prediction of boundary layer transition on a flat plate subject to surface waviness," *Proceedings of the Institution of Mechanical Engineers, Part G: Journal of Aerospace Engineering*, vol. 226, no. 1, pp. 42–54, 2012. DOI: 10.1177/0954410011407268. [Online]. Available: https://doi.org/10.1177/0954410011407268.
- [22] S. Bentley. "Aircraft reduced vertical separation minima (rvsm) skin mapping considerations." Accessed: 01-May-2025. [Online]. Available: https://sassofia.com/blog/aircraft-reduced-vertical-separation-minima-rvsm-skin-mapping-considerations/.
- [23] D. Jin, G. Qian, and K. Feng, "Study on the method of determining skin waviness requirement of civil aircraft," in *Proceedings of the 32nd Congress of the International Council of the Aeronautical Sciences (ICAS)*, Accessed: 29-Apr-2025, Shanghai, China, 2020. [Online]. Available: https://www.icas.org/ICAS_ARCHIVE/ICAS2020/data/papers/ICAS2020_1065_paper.pdf.

- [24] M. Moniripiri, P. P. C. Brito, A. V. G. Cavalieri, N. R. Sêcco, and A. Hanifi, "An adjoint-based methodology for calculating manufacturing tolerances for natural laminar flow airfoils susceptible to smooth surface waviness," *Theoretical and Computational Fluid Dynamics*, vol. 38, no. 1, pp. 15–37, 2024. DOI: 10.1007/s00162-023-00681-y. [Online]. Available: https://link.springer.com/article/10.1007/s00162-023-00681-y.
- [25] B. J. Holmes, C. J. Obara, G. L. Martin, and C. S. Domack, "Manufacturing tolerances for natural laminar flow airframe surfaces," in *General Aviation Aircraft Meeting and Exposition*, SAE Technical Paper 850863, Hampton, VA: SAE International, Apr. 1985. DOI: 10.4271/850863. [Online]. Available: https://ntrs.nasa.gov/citations/19850067952.
- [26] S. F. Hoerner, Fluid-Dynamic Drag: Practical Information on Aerodynamic Drag and Hydrodynamic Resistance. Brick Town, New Jersey: Hoerner Fluid Dynamics, 1965, p. 455, Accessed: 23-Apr-2025, ISBN: 978-9991194448. [Online]. Available: https://ia800606.us.archive.org/17/items/FluidDynamicDragHoerner1965/Fluid-dynamic_drag__Hoerner__1965_text.pdf.
- [27] X. H. Zhang, W. Q. Gong, and C. C. Liu, "Study on multihole pressure probe system based on labview," *Experimental Techniques*, vol. 39, no. 3, pp. 42–54, 2017. DOI: 10.1111/ext.12024. [Online]. Available: https://doi.org/10.1111/ext.12024.
- [28] D. M. Birch, "Multi-hole pressure probes," Surrey Sensors Ltd., Technical Note TN-0616-2016, rev. 1.4b, May 2016. [Online]. Available: https://www.surreysensors.com/wp-content/uploads/2021/05/Multihole-probes.pdf.
- [29] G. L. Morrison, M. T. Schobeiri, and K. R. Pappu, "Five-hole pressure probe analysis technique," Flow Measurement and Instrumentation, vol. 9, no. 3, pp. 153–158, 1998. DOI: 10.1016/S0955-5986(98)00023-5. [Online]. Available: https://doi.org/10.1016/S0955-5986(98)00023-5.
- [30] S. C. C. Bailey et al., "Obtaining accurate mean velocity measurements in high reynolds number turbulent boundary layers using pitot tubes," *Journal of Fluid Mechanics*, vol. 715, pp. 642–670, 2013. DOI: 10.1017/jfm.2012.538. [Online]. Available: https://doi.org/10.1017/jfm.2012.538.
- [31] A. Vasseur, N. Binder, F. Fontaneto, and J.-L. Champion, "Wall-proximity effects on five-hole probe measurements," *International Journal of Turbomachinery, Propulsion and Power*, vol. 9, no. 2, p. 16, 2024. DOI: 10.3390/ijtpp9020016. [Online]. Available: https://www.mdpi.com/2504-186X/9/2/16.
- [32] streamwise gmbh, *ProCap Professional User Manual*, *Version 3.0.2*, Available upon request or via streamwise support, streamwise gmbh, Emil-Staub-Strasse 5, CH-8708 Männedorf, Switzerland, Oct. 2023.
- [33] L. Fan, J. Wang, Z. Xu, and X. Yang, "A reverse modeling method based on cad model prior and surface modeling," *Machines*, vol. 10, no. 10, p. 873, 2022. DOI: 10.3390/machines10100873. [Online]. Available: https://www.mdpi.com/2075-1702/10/10/873.

- [34] M.-J. Rakotosaona, V. L. Barbera, P. Guerrero, N. J. Mitra, and M. Ovsjanikov, "Pointcleannet: Learning to denoise and remove outliers from dense point clouds," *Computer Graphics Forum*, vol. 38, no. 1, pp. 185–203, 2019. DOI: 10.1111/cgf. 13753. [Online]. Available: https://onlinelibrary.wiley.com/doi/10.1111/cgf.13753.
- [35] S. Gonizzi Barsanti, M. R. Marini, S. G. Malatesta, and A. Rossi, "Evaluation of denoising and voxelization algorithms on 3d point clouds," *Remote Sensing*, vol. 16, no. 14, p. 2632, 2024. DOI: 10.3390/rs16142632. [Online]. Available: https://www.mdpi.com/2072-4292/16/14/2632.
- [36] SimScale. "Cfd workflow guide: How to set up a fluid dynamics analysis." Accessed: 27-May-2025. [Online]. Available: https://www.simscale.com/blog/cfd-workflow-quick-guide/.
- [37] Tangent. "3d scan to cad." Accessed: 01-May-2025. [Online]. Available: https://usetangent.com/3d-scan-to-cad/.
- [38] P. Hug, (private communication), 2025.
- [39] B. L. T. Bell and S. Zhang, "Structured light techniques and applications," English, in Wiley Encyclopedia of Electrical and Electronics Engineering, J. G. Webster, Ed., Wiley, 2016, pp. 1–24, ISBN: 9780471346081. DOI: 10.1002/047134608X. W8298. [Online]. Available: https://onlinelibrary.wiley.com/doi/10.1002/047134608X.W8298.
- [40] Smithsonian National Air and Space Museum. "Vortex drag." Accessed: 01-Jun-2025. [Online]. Available: https://howthingsfly.si.edu/aerodynamics/vortex-drag.
- [41] S. Hänzi, (private communication), 2025.

Appendix A

Scanners' Datasheets

Here you will find the datasheets of the scanners used in Chapter 3.4.

Each datasheet includes more technical specifications than the ones shown in Table 3.2 and Table 3.3.

TECHNICAL SPECIFICATIONS

EINSCAN-SE/ SE V2

Model	Einscan-SE	Einscan-SE V2		
Scan Mode	Fixed Scan with Turntable; Fixed Scan without Turntable			
Align Mode	Manually Align; Feature Align; Turntable Align			
Scan Accuracy	≤0.1	mm		
Minimum Scan Volume	30mm × 30m	nm × 30mm		
Maximum Scan Volume	Fixed Scan: 700mm × 700mm × 700 mm	Turntable: 200mm × 200mm × 200mm		
Singe Scan Range	200 mm ×	150 mm		
Scan speed of a single shot	<8s	<1s		
Scan speed of one turn	<2mins	<45s		
Point Distance	0.17mm ~	0.17mm ~ 0.2mm		
Color Scan	Supported			
Output Format	OBJ, STL, ASC, PLY, 3MF			
Camera Resolution	1.3MP			
Light Source	White LED			
Working Distance	290mm ~	480mm		
Power Supply	12V, 3.33A, 40W			
Computer Requirements	OS: Win7, 8, 10 (64bit) CPU: Intel Dual Core i5 or higher; RAM: >8GB Graphics Card: Nvidia GTX660 or higher; Video Memory: >1GB USB Port: 2.0/ 3.0	OS: Win7, 8, 10 (64bit) CPU: Intel Dual Core i5 or higher; RAM: >16GB Graphics Card: Nvidia GTX660 or higher; Video Memory: >2GB USB Port: 2.0/ 3.0		
Device Size	570mm × 210mm			
Package Size	640mm × 410mm × 230mm			
Weight	4.2KG			
Certificate	CE, FCC, ROHS, WEEE			
Calibration Board	Plastic Calibration Board			
Turntable Loading Capacity	5KG			

^{*}Notice: SHINING 3D reserves the right to explain any alteration of the specifications and pictures.

SHINING 3D www.einscan.com sales@shining3d.com

TECHNICAL SPECIFICATIONS

EINSCAN-SP/SP V2

Model	Einscan-SP	Einscan-SP V2	
Scan Mode	Fixed Scan with Turntable; Fixed Scan without Turntable		
Align Mode	Manually Align; Feature Align; Turntable Align; Markers Align; Turntable Coded Target Align		
Scan Accuracy	≤0.05	mm	
Minimum Scan Volume	30mm × 30m	m × 30mm	
Maximum Scan Volume	Fixed Scan: 1200mm × 1200mm × 1200mm Turntable: 200mm × 200mm × 200mm		
Singe Scan Range	200mm ×	150mm	
Scan speed of a single shot	<8s	<1s	
Scan speed of one turn	<2mins	<45s	
Point Distance	0.17mn	n ~ 0.2mm	
Color Scan	Sup	pported	
Output Format	OBJ, STL, A	ASC, PLY, 3MF	
Camera Resolution	1.	3MP	
Light Source	White LED		
Working Distance	290mm ~ 480mm		
Power Supply	12V, 3.33A, 40W		
Computer Requirements	OS: Win7, 8, 10 (64bit) CPU: Intel Dual Core i5 or higher; RAM: >16GB Graphics Card: Nvidia GTX660 or higher; Video Memory: >2GB USB Port: 2.0/ 3.0		
Device Size	570mm × 210mm		
Package Size	640mm × 410mm × 230mm		
Weight	4.2KG		
Certificate	CE, FCC, ROHS, WEEE		
Calibration Board	High Accuracy Calibration Board		
Turntable	With Coded Targets		
Turntable Loading Capacity	5KG		
Attachments	Tripods; Software for Solid Edge SHINING 3D Edition		

^{*}Notice: SHINING 3D reserves the right to explain any alteration of the specifications and pictures. EinScan SE/ SP V2-EN 20220718-V0.2

SHINING 3D www.einscan.com sales@shining3d.com

Micro II Specifications



Accuracy	
3D point accuracy	5 microns, 2 micron repeatability
Accuracy certification	ISO12836
Field of view	
Volume capture	6000 cm³ (18.5 times larger than Micro I)
Field of view	20 × 20 × 15 cm
Scan system	3-axis
Resolution	
Cameras	4 × 13 MP resolution cameras
3D resolution	TBC
Algorithms	
Smart Scanning Mode	Yes
HD Mode	To be released in Artec Studio 19
Color	
Ability to capture texture	Scanner native & phototexture
Colors	24 bpp
Speed	
Data acquisition speed	1 mln points/s
Light source	
3D light source	RGB LED
2D light source	RGB LED

USB 3.0
396 × 405 × 337 mm
12 kg
Windows 10 (x64), Windows 11
Intel Core i7 or i9, 64+ GB RAM, NVIDIA GPU with at least 3 GB VRAM, CUDA 3.5+
Intel Core i5, i7, or i9, 32GB RAM, GPU with 2 GB VRAM
OBJ, PLY, WRL, STL, AOP, ASC, PTX, E57, XYZRGB
STEP, IGES, X_T
CSV, DXF, XML



Appendix

Specifications

Product Name	POP 2 3D Scanner	
Technology	Dual Camera Infrared Light	
Single-frame Precision	Up to 0.05mm	
Single-frame Accuracy	Up to 0.1mm	
Single Capture Range	210mm x 130mm	
Working Distance	150mm - 400mm	
Minimum Scan Volume	20mm x 20mm x 20mm	
Scanning Speed	Up to 10fps	
Light Source	Class 1 Infrared Light	
Alignment	Feature, Marker	
Color Scanning	Yes	
Output Formats	PLY, OBJ, and STL	
Point Distance/Resolution 0.15mm		
Special Object Scanning	Use scanning spray for transparent, dark, or highly reflective objects.	
Scanning Environment	Indoors and Outdoors	
Outdoor Scanning	The POP 2 cannot scan objects well in direct bright sunlight.	
Scanner Weight	195g	
Scanner Dimensions	154.6mm x 38.2mm x 25.6mm	

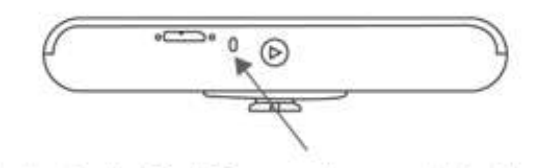
3D Printing Compatible	Yes	
Compatible OS	Windows 10/11 (64-bit), Android,	
Compatible OS	iOS, macOS	
PC Display Screen >1344x768		
Resolution	(1920×1080 is recommended)	
Connection Modes	USB 3.0 or Wi-Fi	
Hardware Button	Start/Pause Scan	

Note: 1. Accuracy was acquired in a controlled lab environment. Actual results might vary, subject to the operation environment.

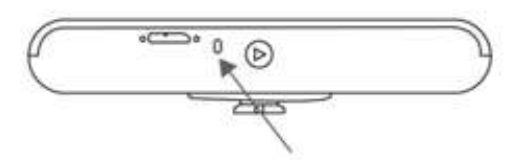
2. Class 1 Laser: Avoid direct eye exposure for extended periods!

Refer to Standards for Class 1 Lasers for details.

LED Indicators



Indicator in Red: Powered on, and starting



Indicator in Green: Working properly

Update the Firmware

When you connect your POP 2 to Revo Scan, a pop-up will notify you of any firmware updates. If you want to update your firmware, follow the install wizard's prompts and ensure that your POP 2 has a stable power supply.

Scanner Calibration

Your POP 2 3D Scanner was calibrated in the factory and only needs to be recalibrated after a year of use or if the scanned results do not match the specified accuracy.

Technical data



ZEISS T-SCAN hawk 2

LLIOU I-OUAH HAWK L	
High-speed scanning	Included (multiple blue laser crosses)
Deep pockets	Included (single blue laser line)
Flexible depth of field	Included (on-object distance radar)
Detailed scan	Included
One-shot sensor recalibration	Included (HyperScale)
Large parts	Included (Satellite mode, no coded markers required)
Carbon-fibre lengths standards	Certified (DaKKs / ILAC) (1)
Volumetric accuracy	0.02mm + 0.015mm/m (2)
9 depth of field	Included (on-object distance radar)
Laser class (IEC 60825-1:2014)	Class 2 (eye-safe)
Weight	< 1kg
Cable	10m (ultra-light)
Software	ZEISS Quality Suite / GOM Inspect
Full remote workflow	Supported

(1) Accreditation Carl Zeiss GOM Metrology SmbH: D-K-21312-01-00 according to DIN EN ISO/IEC17025:2018 (2) Acceptance Test based on ISO 10360

Leica RTC360 LT Product Specifications

GENERAL	
3D laser scanner	High-speed 3D laser scanner with integrated HDR spherical imaging system
PERFORMANCE	
Data acquisition	<3 mins for complete full dome scan and spherical HDR image at 6mm @ 10 m resolution
Double scan	Automatic removal of moving objects
Check & Adjust	Field procedure for targetless checking of angular parameters
SCANNING	
Distance measurement	High-speed, high dynamic time of flight enhanced by Waveform Digitising (WFD) technology
Laser class	1 (in accordance with IEC 60825-1:2014), 1550 nm (invisible)
Field of view	360° (horizontal) / 300° (vertical)
Range	Min. 0.5 - up to 130 m
Speed	Up to 1,000,000 pts / sec
Resolution	3 user selectable settings (3/6/12 mm @ 10 m)
Accuracy*	Angular accuracy 18" Range accuracy 1.0 mm + 10 ppm 3D point accuracy 1.9 mm @ 10 m 2.9 mm @ 20 m 5.3 mm @ 40 m
Range noise* **	0.4 mm @ 10 m, 0.5 mm @ 20 m
IMAGING	
Camera	36 MP 3-camera system captures 432 MPx raw data for calibrated 360° x 300° spherical image
Speed	1 minute for full spherical HDR image at any light condition
HDR	Automatic, 5 brackets
NAVIGATION SENSORS	
Tilt	IMU based, Accuracy: 18" (for upright and upside down setups with +/- 5° inclination)
Additional sensors	Altimeter, Compass, GNSS

OPERATION		
On scanner	Touch-screen control with finger touch, full colour WVGA graphic display 480 x 800 pixels	
Mobile devices	Leica Cyclone FIELD 360 app for iOS and Android tablet computers and smartphones including: - Remote control of scan functions - 2D & 3D data viewing - Tagging - Visual alignment of scans	
Wireless	Integrated wireless LAN (802.11 b/g/n)	
Data storage	Leica MS256, 256 GB exchangeable USB 3.0 flash drive	
DESIGN & PHYSICAL		
Housing	Aluminium frame and sidecovers	
Dimensions	120 mm x 240 mm x 230 mm / 4.7" x 9.4" x 9.1"	
Weight	5.2 kg / 11.5 lbs, nominal (without batteries)	
Mounting mechanism	Quick mounting on 5/8" stub on lightweight tripod / optional tribrach adapter / survey tribrach adapter available	
POWER		
Internal battery	2 x Leica GEB361 internal, rechargeable Li-lon batteries. Duration: Typically up to 4 hours Weight: 340 g per battery	
External	Leica GEV282 AC adapter	
ENVIRONMENTAL		
Operating temperature	-5° to +40°C	
Storage temperature	-40° to +70°C	
Operating low temperatures****	-10° to +40°C	
Dust/Humidity***	Solid particle/liquid ingress protection IP54 (IEC 60529)	







Leica RTC360

Leica Cyclone FIELD 360

Leica Cyclone REGISTER 360



Your Trusted Active Customer Care

Active Customer care is a true partnership between Leica Geosystems and its customers. Customer Care Packages (CCPs) ensure optimally maintained equipment and the most up-to-date software to deliver the best results for your business. The myWorld @ Leica Geosystems customer portal provides a wealth of information 24/7.

All specifications are subject to change without notice.

All accuracy specifications are on a level of confidence of 68% according to the Guide of the Expression of Uncertainty in Measurement (JCGM100:2008) unless otherwise noted.

- * At 89% albedo.
- $\ensuremath{^{**}}$ For single shot measurements
- *** For upright and upside down setups with a +/- 15° inclination

**** Extended low temperature operation is possible to -10° C if internal temperature is at or above -5°C when powered on. For extended low temperature measurement, it is recommended that QA procedures are followed.

Scanner: Laser class 1 in accordance with IEC60825:2014

iPhone and iPad are trademarks of Apple Inc.

Android is a trademark of Google.

Illustrations, descriptions and technical specifications are not binding and may change.

All rights reserved. Printed in Switzerland - Copyright Leica Geosystems AG, Heerbrugg, Switzerland 2019. 897298en - 07.21

Leica Geosystems AG





Powerful and Intuitive Software for Optimal User Experience

VXelements is a powerful integrated 3D software platform that works in complete synergy with the entire fleet of Creaform's 3D measuring devices. With VXelements, both 3D data acquisition as well as post-treatment and analyses occur in the same intuitive interface to guarantee an optimal user experience, seamless interaction with the device, and the shortest time to a usable mesh, 3D model, or inspection report.

Acquisition modules are included with every measurement device from Creaform. They provide real-time visualization and produce better data quality from 3D measurements, making the results user-independent and maximizing device performance. Application modules are available as add-ons to process and optimize 3D scan data for diverse applications, including creating digital twins, product development, reverse engineering, inspections, and dynamic tracking.



Technical Specifications

		MetraSCAN BLACK+™	MetraSCAN BLACK+™ Elite
ACCURACY		0.035 mm (0.0014 in)	0.025 mm (0.0009 in)
VOLUMETRIC ACCURACY	9.1 m ³ (320 ft ³)	0.086 mm (0.0034 in)	0.064 mm (0.0025 in)
	16.6 m ³ (586 ft ³)	0.122 mm (0.0048 in)	0.078 mm (0.0031 in)
AUTOMATIC VOLUME EXTENSION ACCURACY (1)		0.035 mm + 0.020 mm/m (0.0014 in + 0.00024 in/ft)	0.025 mm + 0.015 mm/m (0.0009 in + 0.00018 in/ft)
PROBING ACCURACY WITH HandyPROBE Next+		0.030 mm (0.0012 in)	0.025 mm (0.0009 in)
ACCEPTANCE TEST		Based on VDI/VDE 2634 part 3 and ISO 10360	
SETUP ASSISTANCE TOOLS ⁽²⁾		N/A	Included
MEASUREMENT CAPABILITIES (at a working distance of 0.3 m (1 ft))	Pin	0.750 mm (0.0295 in)	
	Hole	1.250 mm (0.0394 in)	
	Step	0.025 mm (0.009 in)	
	Wall	0.500 mm (0.0197 in)	
LIGHT SOURCE ⁽³⁾	30 blue laser lines (+ 1 extra line)		
SCANNING AREA 310 x 350 mm (12.2 x 13.8 in)		(12.2 x 13.8 in)	
PART SIZE RANGE (recommended)		0.2-6 m (0.7-20 ft)	
WEIGHT		Scanner: 1.49 kg (3.28 lb) Probe: 0.5 kg (1.1 lb) C-Track: 5.7 kg (12.5 lb)	

- (1) The volumetric accuracy performance of the system when using the Automatic Volumetric Extension cannot be superior to the default volumetric accuracy performance for a given model
- $(2) \ \ \text{The Setup Assistance tools enable visual guidances and advanced diagnostics for part and jig setups.}$
- (3) Laser class: 2M (eye safe).



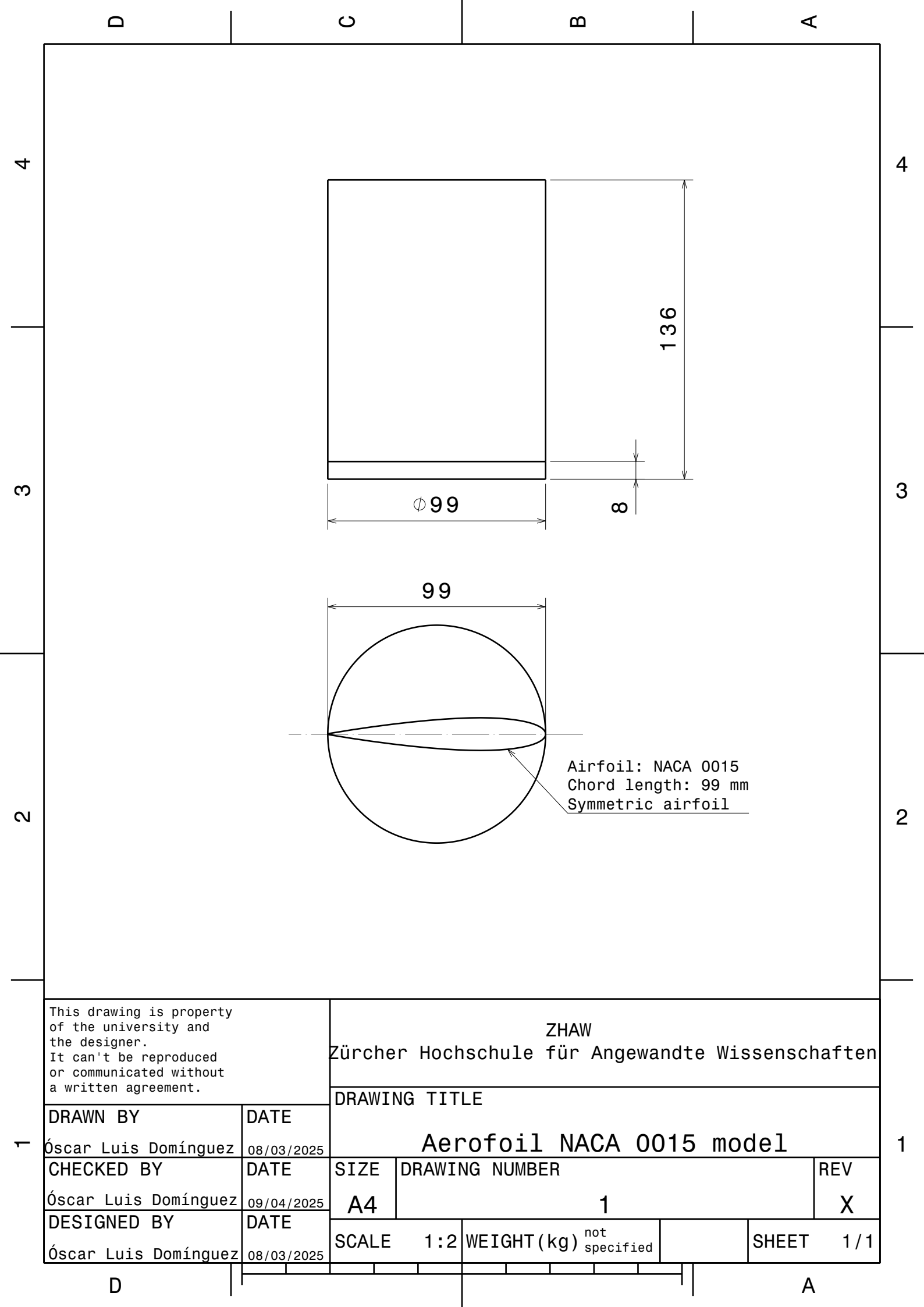
For an unparalleled experience, connect with us at the nearest office located in Canada. $\label{eq:connect}$

creaform3d.com



MetraSCAN 3D, MetraSCAN BLACK+, MetraSCAN BLACK+| Elite, MetraSCAN 357, HandyPROBE, HandyPROBE Next+, VXelements are trademarks of Creaform Inc. © Creaform Inc. 2024. All rights reserved. V1

Appendix B Technical Drawing of the Aerofoil



Appendix C

Creaform HandySCAN 700 Technical specifications

CREAFORM

	HandySCAN 300™	HandySCAN 700™
WEIGHT	0.85 kg (1.9 lbs.)	
DIMENSIONS	77 x 122 x 294 mm (3.0 x 4.8 x 11.6 in.)	
MEASUREMENT RATE	205,000 measurements/s	480,000 measurements/s
SCANNING AREA	225 x 250 mm (8.8 x 9.8 in.)	275 x 250 mm (10.8 x 9.8 in.)
LIGHT SOURCE	3 laser crosses	7 laser crosses (+1 extra line)
LASER CLASS	2M (eye-safe)	
RESOLUTION	0.100 mm (0.0039 in.)	0.050 mm (0.0020 in.)
ACCURACY	Up to 0.040 mm (0.0016 in.)	Up to 0.030 mm (0.0012 in.)
VOLUMETRIC ACCURACY*	0.020 mm + 0.100 mm/m (0.0008 in. + 0.0012 in./ft)	0.020 mm + 0.060 mm/m (0.0008 in. + 0.0007 in./ft)
VOLUMETRIC ACCURACY (WITH MaxSHOT 3D)*	0.020 mm + 0.025 mm/m (0.0008 in. + 0.0003 in./ft)	
STAND-OFF DISTANCE	300 mm (11.8 in.)	
DEPTH OF FIELD	250 mm (9.8 in.)	
PART SIZE RANGE (RECOMMENDED)	0.1 – 4 m (0.3 – 13 ft)	

	HandySCAN 300™	HandySCAN 700™	
SOFTWARE	VXele	VXelements	
OUTPUT FORMATS	.dae, .fbx, .ma, .obj, .ply, .stl, .txt, .wrl, .x3d, .x3dz, .zpr		
COMPATIBLE SOFTWARE	3D Systems (Geomagic® Solutions), InnovMetric Software (PolyWorks), Dassault (CATIA V5 and SolidWorks), PTC (Pro/ENGINEER), Siemens (NX and Solid Edge), Autodesk (Inventor, Alias, 3ds Max, Maya, Softimage).		
CONNECTION STANDARD	1 X USB 3.0		
OPERATING TEMPERATURE RANGE	5-40 °C (41-104 °F)		
OPERATING HUMIDITY RANGE (NON-CONDENSING) 10-90%		90%	